RELAZIONE ANNUALE SULL'ATTIVITA' SVOLTA

Nell'ambito della borsa di dottorato aggiuntiva del Programma Operativo Nazionale Ricerca e Innovazione 2014-2020 (CCI 2014IT16M2OP005), Fondo Sociale Europeo, Azione I.1 "Dottorati Innovativi con caratterizzazione Industriale"

Dottorando	Minh Long Hoang
Tutor	Antonio Pietrosanto
Coordinatore	Francesco Donsi
Corso di Dottorato	Ingegneria Industriale
Ciclo	XXXIV
Annualità della borsa	3
Codice borsa e n.	DOT1328711 - Borsa: 3
CUP	D44J18000280006
Titolo Progetto	Industry-Oriented Enhancement of Inertial Platform Performance

In piena coerenza con le attività previste dal progetto nell'ambito del quale è stata finanziata la borsa di dottorato, si presenta la relazione annuale dell'attività svolta.

OGGETTO:

In this work, robust mechanical setup and highly effective algorithms have been proposed to optimize the performance of the inertial measurement unit (IMU) in orientation tracking. This work aims to develop new techniques to minimize the noise as well as the weakness of Euler angles measurement in the industry. The imperfect structure and limit of low-cost accelerometer, gyroscope, and magnetometer with external interferences significantly decrease the precision of roll, pitch, and yaw. A new algorithm, No Motion No Integration (NMNI), was developed to eliminate the gyroscope drift, which opened a new way to calculate the yaw/heading value without magnetometer and Global Positioning System (GPS). Moreover, the NMNI method successfully improved the inclination outputs from sensor fusion Madgwick and Mahony. To deal with external vibration, another technique Orientation Axes Crossover Processing (OACP), has been applied on vibration optimization for Microelectromechanical systems (MEMS) accelerometer without sensor fusion. The proposed filter works on a principle based on the characteristics of vibration impact on whether the X-axis or Y-axis to optimally minimize the noise. The results were validated carefully with a mechanical test bench, based on a Pan-Tilt Unit-C46 (PTU-C46) with accurate positioning as reference angles for static and dynamic experiments. In the company activity, a robust orientation system for inclinometer with full

redundancy was described. The designed structure provides high efficiency for inclinometer performance with tolerance of ±0.2°, and stability is always guaranteed thanks to safety function, which is strongly recommended for the application of heavy industry.

Data: 22/02/2022

Firma dottorando:

Industry-Oriented Enhancement of Inertial Platform Performance

Minh Long Hoang

UNIVERSITY OF SALERNO

DEPARTMENT OF INDUSTRIAL ENGINEERING

Ph.D. Course in Industrial Engineering
Curriculum in Electronic Engineering - XXXIV Cycle

INDUSTRY- ORIENTED ENHANCEMENT OF INERTIAL PLATFORM PERFORMANCE

Supervisor
Prof. Antonio Pietrosanto

Ph.D. student
Minh Long Hoang

Scientific Referees
Prof. Luca De Vito
Prof. Lorenzo Ciani

Ph.D. Course Coordinator
Prof. Francesco Donsì

Publications resulting from this work

Hoang, M.L. and Pietrosanto, A. (2021). New Artificial Intelligence Approach to Inclination Measurement based on MEMS Accelerometer. IEEE Transactions on Artificial Intelligence,2021. DOI: 10.1109/TAI.2021.3105494.

Hoang, M.L. and Pietrosanto, A. (2021). Yaw/Heading optimization by drift elimination on MEMS gyroscope. Sensors and Actuators A: Physical, 325, p.112691. DOI: 10.1016/j.sna.2021.112691

Hoang, M.L., Carratù, M., Paciello, V. and Pietrosanto, A. (2021). Body Temperature—Indoor Condition Monitor and Activity Recognition by MEMS Accelerometer Based on IoT-Alert System for People in Quarantine Due to COVID-19. Sensors, 21(7), p.2313. DOI: 10.3390/s21072313

Hoang, M.L. and Pietrosanto, A. (2021). A Robust Orientation System for Inclinometer With Full-Redundancy in Heavy Industry. IEEE Sensors Journal, 21(5), pp.5853–5860. DOI: 10.1109/JSEN.2020.3040374.

Hoang, M.L., Iacono, S.D., Paciello, V. and Pietrosanto, A. (2021). Measurement Optimization for Orientation Tracking Based on No Motion No Integration Technique. IEEE Transactions on Instrumentation and Measurement, 70, pp.1–10. DOI: 10.1109/tim.2020.3035571

Hoang, M.L. and Pietrosanto, A. (2021). A New Technique on Vibration Optimization of Industrial Inclinometer for MEMS Accelerometer Without Sensor Fusion. IEEE Access, 9, pp.20295–20304. DOI: 10.1109/ACCESS.2021.3054825.

Hoang, M. L., Carratù, M., Paciello, V. and Pietrosanto, A. (2021) “Noise attenuation on IMU measurement for drone balance by sensor fusion,” in 2021 IEEE International Instrumentation and Measurement Technology Conference (I2MTC). IEEE. DOI: 10.1109/I2MTC50364.2021.9460041.

Hoang, M.L., Carratu, M., Ugwiri, M.A., Paciello, V. and Pietrosanto, A. (2020). A New Technique for Optimization of Linear Displacement Measurement based on MEMS Accelerometer. 2020 International Semiconductor Conference (CAS). DOI: 10.1109/CAS50358.2020.9268038.

Hoang, M.L., Pietrosanto, A., Iacono, S.D. and Paciello, V. (2020). Pre-Processing Technique for Compass-less Madgwick in Heading Estimation for Industry 4.0. 2020 IEEE International Instrumentation and Measurement Technology Conference (I2MTC). DOI: 10.1109/I2MTC43012.2020.9128969

Hoang, M.L. and Pietrosanto, A. (2020). An Effective Method on Vibration Immunity for Inclinometer based on MEMS Accelerometer. 2020 International Semiconductor Conference (CAS). DOI: 10.1109/CAS50358.2020.9267997

Carratu, M., Iacono, S.D., Long Hoang, M. and Pietrosanto, A. (2019). Energy characterization of attitude algorithms. 2019 IEEE 17th International Conference on Industrial Informatics (INDIN). DOI: 10.1109/INDIN41052.2019.8972300.

Hoang, M.L., Carratu, M., Paciello, V. and Pietrosanto, A. (2020). A new Orientation Method for Inclinometer based on MEMS Accelerometer used in Industry 4.0. 2020 IEEE 18th International Conference on Industrial Informatics (INDIN). DOI: 10.1109/indin45582.2020.9442189.

Contents

List of figures

List of tables

Abstract

In this work, robust mechanical setup and highly effective algorithms have been proposed to optimize the performance of the inertial measurement unit (IMU) in orientation tracking. This work aims to develop new techniques to minimize the noise as well as the weakness of Euler angles measurement in the industry. The imperfect structure and limit of low-cost accelerometer, gyroscope, and magnetometer with external interferences significantly decrease the precision of roll, pitch, and yaw. A new algorithm, No Motion No Integration (NMNI), was developed to eliminate the gyroscope drift, which opened a new way to calculate the yaw/heading value without magnetometer and Global Positioning System (GPS). Moreover, the NMNI method successfully improved the inclination outputs from sensor fusion Madgwick and Mahony. To deal with external vibration, another technique, named as Orientation Axes Crossover Processing (OACP), has been applied on vibration optimization for Microelectromechanical systems (MEMS) accelerometer without sensor fusion. The proposed filter works on a principle based on the characteristics of vibration impact on whether the X-axis or Y-axis to optimally minimize the noise. The results were validated carefully with a mechanical test bench, based on a Pan-Tilt Unit-C46 (PTU-C46) with high accurate positioning as reference angles for static and dynamic experiments. In the last part, a robust orientation system for inclinometer with full redundancy was described, which was carried out at the Industrial Inclinometer Company. The designed structure provides high efficiency for inclinometer performance with tolerance of $\pm 0.2^{o}$, and stability is always guaranteed thanks to safety function. The designed inclinometer was used for a real excavator to verify its stability and operating performance.

Introduction

IMUs are self-contained systems that provide the angular position by rate-integrating gyroscope, a linear accelerometer and a magnetometer. MEMS IMU and attitude and heading reference system can provide accurate orientation under the most demanding conditions (Hoang, Iacono, Paciello, & Pietrosanto, 2021), (Hoang, Carratu, Paciello, & Pietrosanto, 2021). The advancing technology for orientation tracking (Carratu, Iacono, Hoang, & Pietrosanto, 2019), (Harindranath & Arora. 2018), (Huyghe, Doutreloigne, & Vanfleteren, 2009) has been developing dramatically for the wide-range application in the industry, especially in automation (Lan, Bu, Liang, & Hao, 2016), (Kong, 2004) and industrial safety (Qinglei, Huawei, Shifu & Jian 2007), (Da-wei & Tao, 2011) .

Roll, pitch and yaw are the three quantities used for orientation tracking: rotation around the front-to-back axis is called roll; rotation around the side-to-side axis is called pitch; rotation around the vertical axis is called yaw.

The inclination like roll and pitch can be measured by using MEMS accelerometer and gyroscope despite of significant issues. The accelerometer can provide the proper data for the users but noise from the external interference negatively affects its accuracy especially in a vibrating environment such as in a car or an airplane. A gyroscope offers angular velocities around the three axes and the signals are not susceptible to external forces comparing to accelerometers. However, gyroscope data have a tendency to drift because of the angular velocity data bias accumulation over time. There are sensor fusion algorithms such as Madgwick, Mahony and Kalman which are good solutions to enhance the acquired results. Nevertheless, the limit of accuracy still present, so the company demand higher precision of the tracking angles. Furthermore, the yaw has become a big challenge for IMU since the accelerometer cannot provide the yaw information when the sensor frame is aligned with the Earth frame. The Z-axis acceleration does not change its reading value when the sensor rotates tothe right or left. The magnetometer's support has been applied popularly to overcome this accelerometer's weakness (Helbling, Fuller & Wood, 2014), (Shi, Li & Jiang, 2018). However, magnetometer requires the high – precision calibration for hard iron as well as soft iron that increases the complexity of

the system and also requires the assistance of the GPS (Carratu, Iacono, Pietrosanto & Paciello, 2019), (Wahyudi, Listiyana, Sudjadi & Ngatelan, 2018) to guarantee the accuracy of yaw, especially when the strange magnetic distortion appears while the calibration is not updated yet. The scientists already examined the considerable cons of GPS such as Signal Multipath, Receiver and Orbital Clock error. Environmental problems like Ionospheres delay because of the distance and delay in time caused the low accuracy in result (Damani , Shah, Shah & Vala, 2015). On the other hand, GPS works less effectively in the indoor environment that causes the problem for indoor applications.

The gyroscope can reach the yaw 's actual value for a short time, but unfortunately, the 'drift' phenomenon leads to erroneous data. Therefore, the No Motion No Integration (NMNI) technique was presented with the real-time operation to prevent any single portion of drift. With NMNI method, each time the gyroscope stays at static state, its drift is eliminated to zero. The NMNI filter directly works on the gyroscope drift's main problem based on a threshold between stationary state and motion state to prevent the yaw calculation from the additional portion integration. The principle "No Motion No Integration" and "Renovating Model" construct a real-time operation for the whole system to significantly strengthen the gyroscope characteristic in orientation tracking. The proposed filter combines with Madgwick and Mahony (Hoang, Iacono, Paciello, & Pietrosanto, 2021) to become filter fusion, which optimize not only yaw but also roll and pitch.

On the other hand, many companies desire to develop the inclinometer with solely MEMS accelerometer to reduce the platform cost, but still guarantee high performance. Hence, the research also focuses on the efficiency maximization of inclination (roll, pitch) by using only accelerometer. Another new algorithm Orientation Axes Crossover Processing (OACP) was invented to minimize the external vibration on inclinometer during industrial operation.

The proposed filter works on a principle based on the characteristics of vibration impact on whether the X-axis or Y-axis to optimally minimize the noise. A high accurate setup is built-up based on the Pan-Tilt Unit and a TUMAC vibrator for the verification of new filters, implemented into LSM9DS1 (3D accelerometer, 3D gyroscope). The new filter is able to work independently, and also fuse with the Low-pass filter or Kalman filter to enhance the dynamic response, only 0.163 seconds as maximum delay during vibration (Hoang, & Pietrosanto, 2021).

Finally, in the company 'Sensor System', a robust orientation system for industrial inclinometer based on Microelectromechanical Systems (MEMS) accelerometer has been studied and developed. The inclinometer is calibrated based on an industrial motor (Vexta), as an oriental reference. The STM microcontroller (MCU) has the role of memorizing the inclination sent from the motor with the corresponding acceleration into a Lookup Table (LUT) by using Flash memory. The full redundancy included dual accelerometers and

MCUs to enhance the safety function for the operating system via two inclination channels. The support from the Low-pass filter and the zero-offset compensation for temperature change contribute to the measurement precision. For industrial applications, Control Area Network open (CANopen) is used as an embedded network communication system. The precise tests were carried out to verify the behavior of the inclination sensor (Hoang, & Pietrosanto, 2021). The full redundancy inclinometer can guarantee both precision and safety function for the users.

The thesis is organized as follow: Firstly, the description of IMU sensors and orientation angles are presented. Next, the sensor fusion will be depicted with their pros and cons and the proposed algorithm NMNI are demonstrated. After this part, the work concentrates on the optimization of inclinometer with only accelerometer. The vibration immunity filter OACP is described, showing an optimized approach to inclination measurement. Last but not least, research activity in company is reported with robust calibration setup and full redundancy inclinometer.

Chapter I
Orientation angles and IMU sensors

Nowadays, the demand of high accuracy of orientation tracking has increased drasmatically due to its wide-range applications in automation and industry 4.0 (Hoang, Pietrosanto, Iacono & Paciello, 2020). The IMU sensors play the key role in acquiring these oriental data. Accelerations can be converted to the roll and pitch via the trigonometric formula (Christopher, 2010). Angular rates integration from gyroscope also can provide the oriental results. Magnetometer has the function of yaw/heading detection. The calibration for these sensors is required to compensate for the imperfection of manufactured structure and the noise. The main features and signal characteristics of these sensor will be introduced.

I.1 Axis and rotation definition

The orientation tracking refers to Euler angles, which contains three quantities roll, pitch and yaw as illustrated in Figure I.1.

- Roll is rotation around the front-to-back axis.
- Pitch is rotation around the side-to-side axis.
- Yaw is rotation around the vertical axis.

These 3 quantities are highly concerned because only small error can cause the considerable issues to the whole operating system.

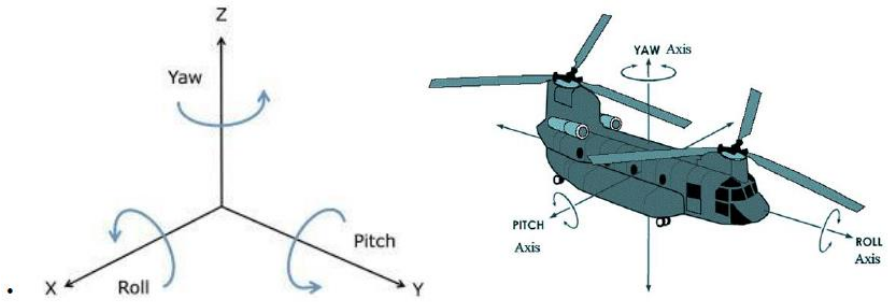

Figure I.1 *Euler angles on three axes*

I.2 IMU sensor in angle detection

I.2.1 Accelerometer

An accelerometer is an electromechanical device used to measure acceleration forces, static angle of tilt or inclination. Such forces may be static, like the continuous force of gravity or, as is the case with many mobile devices, dynamic to sense movement or vibration.

Acceleration is the measurement of the change in velocity, or speed divided by time. To measure roll and pitch, 2 fundamental formulas can be used to calculate the oriental inclination (Promrit,Chokchaitam & Ikura, 2018), (Cocco, & Rapuano, 2007). The axis angles on accelerometer are illustrated as Figure I.3. The X-axis acceleration (Xacc) is proportional to the sine of the angle of inclination (Roll) (Figure I.2). The Y-axis acceleration (Yacc) is calculated by the cosine of the inclination (Pitch) as (I.1) and (I.2).

$$\text{Roll} = \arcsin(\text{Xacc}) \quad \text{(I.1)}$$

$$\text{Pitch} = \arccos(\text{Yacc}) - 90^0 \quad \text{(I.2)}$$

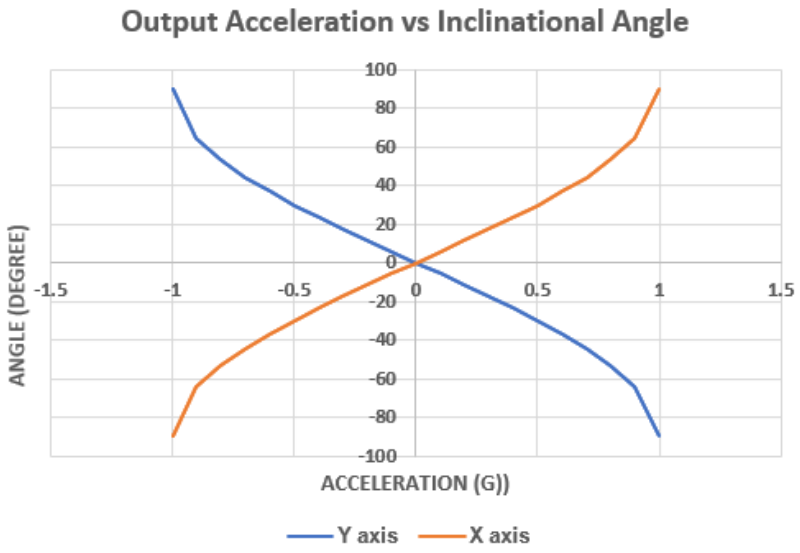

Figure I.2 *Acceleration vs angle*

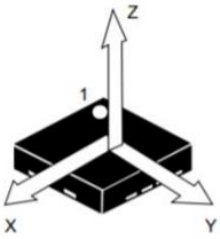

Figure I.3 *(Top view) direction of the detectable accelerations*

At this point, the acceleration data should be calibrated. When the errors due to offset and sensitivity mismatch are combined, the error can become quite large and well beyond the acceptable limits in an inclination sensing application. To reduce this error, the offset and sensitivity are calibrated, and the calibrated output acceleration used to calculate the angle of inclination. When including the effects of offset and sensitivity, the accelerometer output is as follows:

$$A_{OUT}\,[g] = A_{OFF} + (Gain * A_{ACTUAL}) \qquad (I.3)$$

Where: A_{OFF} is the offset error, in g. Gain is the gain of the accelerometer, ideally a value of 1. A_{ACTUAL} is the real acceleration acting on the accelerometer and the desired value, in g.

Ideally, without any inclination, each axis which vertically stays on the Earth frame, outputting the acceleration of 1g and it becomes -1g when reversing the sensor. Figure I.3 shows the Z axis, which stays vertically respects to the Earth frame (STMicroelectronics, 2019).

When an axis is placed into a +1 g and −1 g field, the measured outputs are as follows:

$$A_{+1g}\,[g] = A_{OFF} + (1\ g * Gain) \tag{I.4}$$

$$A_{-1g}\,[g] = A_{OFF} - (1\ g * Gain) \tag{I.5}$$

Where the offset, A_{OFF}, is in g.

Taking the sum of eq (I.4) and (I.5), the new equation is generated:

$$(A_{+1g} + A_{-1g}) = 2\ A_{OFF} \tag{I.6}$$

$$A_{OFF}\,[g] = 0.5 * (A_{+1g} + A_{-1g}) \tag{I.7}$$

Substituting eq (I.7) into (I.4), we have:

$$A_{+1g}\,[g] = 0.5 * (A_{+1g} + A_{-1g}) + Gain \tag{I.8}$$

$$0.5 \times A_{+1g} - 0.5 * A_{+1g} = Gain \tag{I.9}$$

Now, the Gain is achieved as below:

$$Gain = 0.5 * \frac{A_{+1g} - A_{-1g}}{1g} \tag{I.10}$$

This calibration aims to remove the offset and acceleration mismatch during manufactured process. These values would be used by first subtracting the offset from the accelerometer measurement and then dividing the result by the gain

$$A_{ACTUAL} = 0.5 \times \frac{A_{OUT} - A_{OFF}}{GAIN} \tag{I.11}$$

I.2.2 Gyroscope

Gyroscope measures angular velocity, based on a small resonating mass attached to the MEMS which is shifted as the angular velocity changes. Then, output movement is converted to a small electronic signal, which is then amplified and read by a controller around the axes in X-Y-Z directions.

To calculate the orientation angles, the integration method is applied to yield the final data on each axis.

$$\text{Angle} = \int_{t1}^{t2} \omega * \mathrm{t}\ dt \qquad \text{(I.12)}$$

Where angle is roll, pitch and yaw, integrated by angular data ω_x, ω_y and ω_z from X, Y, Z axis respectively.

During the integration process, the gyroscope suffers significant drift overtime, especially when gyroscope stays at the static state. The sensor finishes its motion, but the angular velocity is still continue to be added to the angle measurement that leads to the wrong result.

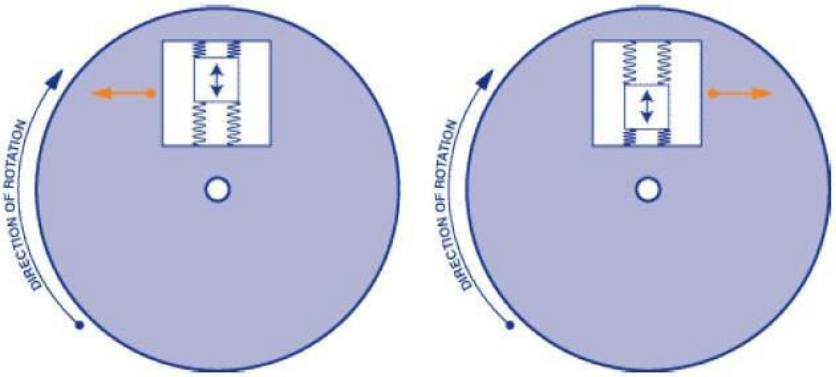

Figure I.4 *Gyroscope rotation motion*

Therefore, the gyroscope calibration is aimed to minimize the drift in angular velocity. The fundamental method is to place the gyroscope on the static state at the starting period. Firstly, N samples are extracted from ω_x, ω_y and $\omega_{z.}$ Then, the average value of each axis value will be calculated to be extracted from all the next acquisition data.

$$\omega_{\text{bias}} = \frac{\sum_{i=1}^{N} \omega_i}{N} \qquad \text{(I.13)}$$

$$\omega_{\text{cal}} = \omega - \omega_{\text{bias}} \qquad \text{(I.14)}$$

Where ω_{bias} is the bias value, ω_{cal} is calibrated data. Usually, N can be set as 100, which is corresponding sample number for calibration.

I.2.3 Magnetometer

Magnetometer measures the magnetic field's strength in a position. From that the heading/yaw angle is determined. The Earth is a giant magnet with the two North and South poles on two sides as shown in Figure I.5. Based on the magnetometer value, the yaw angle can be calculated as:

$$\text{Yaw} = tan^{-1}\left(\frac{m_x}{m_y}\right) \quad \text{(I.15)}$$

Where m_x, m_y are magnetic field measured surround axis x, axis y respectively.

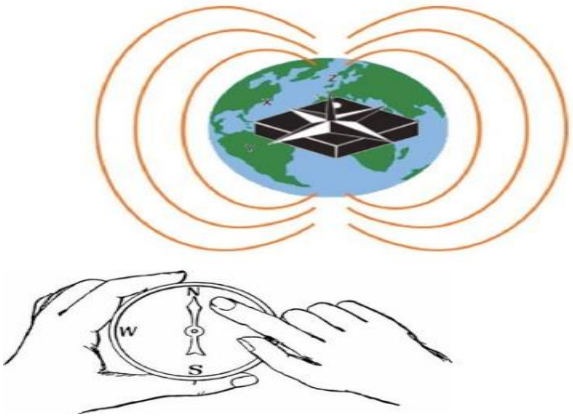

Figure I.5 *MEMS magnetometer*

When the magnetometer rotates in clockwise, the yaw angle is supposed to increase, and decreases for the opposite direction. However, the iron distortion usually interferes the magnetometer performance. Hard iron from the magnetized material or external magnet moves the magnetic sphere away from original center coordinate. Soft iron from metallic material such as nickel battery deforms the magnetic field's shape, which results in the wrong value in data acquisition. Thus, the magnetometer calibration is highly required to remove the bias and offset the measured data (Hu, F. *et al.* 2019).

The ideal response surface for a three-axis magnetometer is a sphere centered at the 3 D origin. It means that no matter the orientation of the magnetometer is a sphere with the same radius centered on the origin. In practice, MEMS magnetometers are rarely so well calibrated when you receive them. There are good reasons for this. The MEMS sensors are

typically characterized at the factory but mounting on a PC board can add stresses that can easily result in a shift of the calibration.

There are various types of magnetometer calibration. In this chapter, we will discuss about a calibration method, which is simple but still effective with low-cost MEMS magnetometer such as MPU9250, LSM9DS1, etc.

To correct the iron biases, the users have to record a numerous magnetometer data as the sensor is moved slowly in a figure eight pattern and keep track of the minimum and maximum field measured in each of the six principal directions: +/- m_x, +/- m_y, +/- m_z. Once the min/max values along the three axes are known, the average can be subtracted from the subsequent data which amounts to re-centering the response surface on the origin.

- Hard iron bias (m_{hard}) calculation:

$$m_{hard} = \begin{pmatrix} m_{hard\_x} \\ m_{hard\_y} \\ m_{hard\_z} \end{pmatrix} = \frac{1}{2} \begin{pmatrix} \max(m_x) + \min(m_x) \\ \max(m_y) + \min(m_y) \\ \max(m_z) + \min(m_z) \end{pmatrix} \quad \text{(I.16)}$$

- Soft iron bias(m_{soft}) calculation:

The computed min/max values are used to rescale the magnetometer data to equalize the response along the three measurement axes. A scale factor is calculated by taking the ratio of the average from the difference between max and min value (max – min) along each axis and the average of all three axes. By this way, an axis where the max - min is large has its magnetic field reduced and an axis which under-measures the field with respect to the other axes has its magnetic field values increased. This technique is a orthogonal rescaling, equivalent to a diagonalized 3 x 3 calibration matrix but it allows some additional correction for scale bias. The cost of correcting for scale bias in this way is small, compared to the much more mathematically formidable ellipsoidal error corrections employed in the most sophisticated algorithms.

Step1: Scale of each axis calculation (m_{scale})

$$m_{scale} = \begin{pmatrix} m_{scale\_x} \\ m_{scale\_y} \\ m_{scale\_z} \end{pmatrix} = \frac{1}{2} \begin{pmatrix} \max(m_x) - \min(m_x) \\ \max(m_y) - \min(m_y) \\ \max(m_z) - \min(m_z) \end{pmatrix} \quad \text{(I.17)}$$

Step2: Average of 3 axes scale (m_{AS})

$$m_{AS} = \frac{m_{scale\_x} + m_{scale\_y} + m_{scale\_z}}{3} \quad \text{(I.18)}$$

Step3: Collecting the m_{soft}

$$m_{soft} = \begin{pmatrix} m_{soft\_x} \\ m_{soft\_y} \\ m_{soft\_z} \end{pmatrix} = \begin{pmatrix} m_{AS}/m_{scale\_x} \\ m_{AS}/m_{scale\_y} \\ m_{AS}/m_{scale\_z} \end{pmatrix} \quad \text{(I.19)}$$

Eventually, the magnetic data (m_{cal})are calibrated as follow:

$$m_{cal} = \begin{pmatrix} m_{soft\_x}\,(m_x - m_{hard_x}) \\ m_{soft\_y}\,(m_y - m_{hard_y}) \\ m_{soft_z}(m_z - m_{hard_z}) \end{pmatrix} \quad \text{(I.20)}$$

After the calibration, the magnetometer acquisition works appropriately. However, if there are new external distortion appears suddenly that can impact on the data negatively. Therefore, the alternative solution for yaw is to optimize the gyroscope drift, which will be discussed in the chapter III.

Chapter II
Sensor fusion Algorithms

Sensor fusion technique collects the data from various sensors to bring out a better result with less noise and adjusted accuracy. In the orientation field, there are several algorithms, which are used popularly: Complementary filter, Kalman filter, Madgwick and Mahony filter. Each algorithm has its own advatnages and disadvantages due to their different working principle and operating structure.

II.1 Complementary filter

A complementary filter is a simple, common way to fuse the gyroscope and accelerometer to obtain accurate pitch, roll and yaw attitude outputs. It is developed in such a way that the strength of one sensor will be used to overcome the weaknesses of the other sensor, which is complementary to the other and hence the name of the filter. On the other hand, IMU that consists of a gyroscope and accelerometer provides more accurate motion measurements at higher speeds since it measures the time derivatives with a low-pass filter for the accelerometer data and a high pass filter for the gyroscope signal (Maxudov, Ercan & Erdem, 2015), (Ariffin, Arsad, & Bais, 2016). The filter is easier to implement and to understand compared to the Kalman filter which is often used for inertial navigation system. The gyroscope is not influenced by external forces so it can reach high accuracy of data for a short term then the drift problem affects its performance. In contrast, the accelerometer data do not drift but the noise impact from environment may affect its positioning capacity. Based on their characteristics, the combination among 3D accelerometers and 3D gyroscopes brings the reliable outcome to users.

$$\theta = \alpha * \theta_{Gyro} + (1 - \alpha) * \theta_{Acc} \quad \text{(II.1)}$$

Where α is the weight of gyro angle, which indicates the percentage number of gyroscope value in the measured angle. (Euston, *et al.* 2008).

For the low-pass filter, signals that are much longer than the time constant can pass the filter unaltered while signals shorter than the time constant are filtered out. The opposite is also true for the high-pass filter. A block diagram of a simple sensor fusion-algorithm based on complementary filter is shown below in Figure II.1.

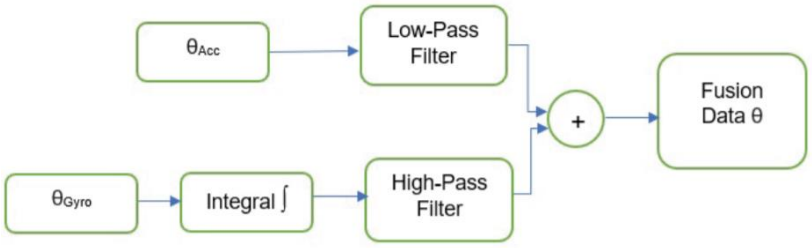

Figure II.1 *Complementary Filter Scheme*

II.2 Kalman filter

Kalman filter is a useful tool to remove the random noise by using the prediction and update (Brunner, *et al,* 2015). In this case, the angular velocity fuses with the acceleration to reduce the conducted noise in the calculated inclination.

Kalman model:

$$x[k+1] = Bx[k] + x[k] \quad \text{(II.2)}$$

$$z[k] = Hx[k] + v[k] \quad \text{(II.3)}$$

Where x[k], x[k+ 1] are the state vector respectively at time k and k + 1, B is the state transition matrix, w[k] is the state transition noise, z[k] is the measurement of x at time k, H is the observation matrix and v[k] is the measurement noise

State variable x is a physical quantity. In case of attitude estimation, it can be velocity, position or an angle. For each Euler angle the Kalman filter can be applied separately, in this case the x state will contain the angle θ and the bias θ_{bias} based upon the measurements from the accelerometer and gyroscope (II.4)

$$x[k] = \begin{bmatrix} \theta \\ \theta_{bias} \end{bmatrix} \quad \text{(II.4)}$$

The state transition matrix can be expressed as in (II.5).

$$B = \begin{bmatrix} 1 & -\Delta T \\ 0 & 1 \end{bmatrix} \quad \text{(II.5)}$$

The H matrix is used to map the true state into the observed state and is formed as in (II.6).

$$H = [1\ 0] \quad \text{(II.6)}$$

For the Kalman filter, the state transition noise matrix w[k] and the measurement noise v[k] need to be considered as random variable with a zero mean Gaussian distribution.

$$w[k] \sim N(0, Q_k) \quad \text{(II.7)}$$

$$v[k] \sim N(0, R) \quad \text{(II.8)}$$

Where Q[k] is the process noise covariance matrix and R can be evaluated as the variance of the measurements. This matrix is composed of the estimated state from the accelerometer variance Qacc and the variance of bias Qbias multiplied by the time interval ΔT, as (II.9).

$$Q[k] = \begin{bmatrix} Qacc & -\Delta T \\ 0 & Qbias \end{bmatrix} \quad \text{(II.9)}$$

If the estimation is slow, Qacc should be decreased to make the algorithm more responsive, meanwhile Qbias is supposed to be increased when the estimated angle starts to drift. In case the measurement noise variance is too high, the filter will respond slowly as it is trusting on the new measurements less, but if it is too small the value might overshoot and be noisy since the algorithm gives too high weight to the accelerometer measurements.

The Kalman operation includes six main steps as Figure II.7.

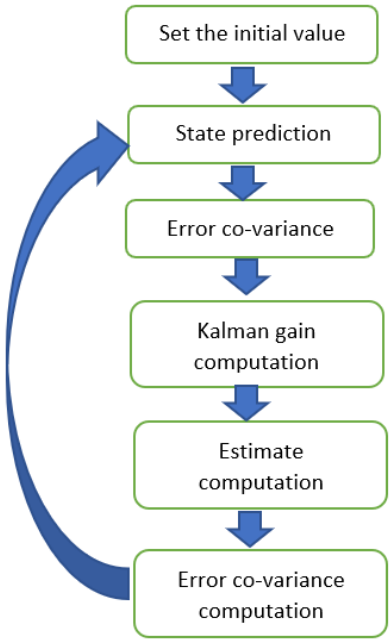

Figure II.2 *Kalman operating principle*

Step 1: The initial values are set up where time k =0. The error covariance matrix P in our case is a two-by-two matrix. The true state of the system is regarded as symbol $\hat{x}$

$$\hat{x}[0] = 0 \tag{II.10}$$

$$\mathrm{P}\,[0] = \begin{bmatrix} P_{00} & P_{01} \\ P_{10} & P_{11} \end{bmatrix} \tag{II.11}$$

Step 2: State prediction is evaluated. The filter starts estimating the current state based on all the previous states and the gyro measurement. The superscript '-' indicates predicted value.

$$\hat{x}[\mathrm{k}]^{-} = \mathrm{B}\hat{x}\,[\mathrm{k}-1] \tag{II.12}$$

Step 3: Error co-variance prediction is processed. This step uses error covariance from the previous time point to estimate the error covariance at the current time point.

$$\mathrm{P}[\mathrm{k}]^{-} = \mathrm{BP}\,[\mathrm{k}-1]\,\mathrm{B}^{\mathrm{T}} + \mathrm{Q}[\mathrm{k}] \tag{II.13}$$

Step 4: Kalman gain is computed. H and R matrices are computed outside the filter, and $P[k]^-$ comes from the previous step. Kalman gain is the weight used for the computation of the estimation and it updates for each time step based on error covariance.

$$K[k] = P[k]^- H^T (HP[k]^- H^T + R)^{-1} \quad \text{(II.14)}$$

For the 6-degree of freedom IMU case, the Kalman gain is a 2 by 1 matrix:

$$K = \begin{bmatrix} K_0 \\ K_1 \end{bmatrix}$$

Step 5: The estimation is optimized. The algorithm compensates the difference between measurement and prediction. This is the output of the filter

$$\hat{x}[k] = \hat{x}[k]^- + K[k]\, H\, (z[k] - H\, \hat{x}[k]^-) \quad \text{(II.15)}$$

After this step, the algorithm re-executes from step 2 continuously.

II.3 Madgwick and Mahony filter

The attitude represents the orientation of a body in the space as Figure I.1. In Madgwick and Mahony algorithm, instead of the Euler angles, quaternions are used for the calculation of attitude filters. This representation form overcomes the problem of gimbal lock and ambiguous representation of the Euler angles. A quaternion can be written as a vector with four elements as follows:

$$q = (q_0, q_1, q_2, q_3) \quad \text{(II.16)}$$

Unit quaternions, quaternions with a unit norm, can be used to represent the attitude of a body. The definition of transformation goes behind the scope of this thesis; more information about quaternions and Euler angles and rotation sequences can be found in (Diebel.J. 2006), (Kuipers, (2020). The quaternion representation can be converted to the Euler angles by using the following equations:

$$\text{roll} = \arctan\left(\frac{q_0 q_1 + q_2\, q_3}{q_0^2 - q_1^2 - q_2^2 + q_3^2}\right) \quad \text{(II.17)}$$

$$\text{pitch} = \arcsin\left(2 * (q_1 q_3 - q_0\, q_2\right) \quad \text{(II.18)}$$

$$\text{yaw} = \arctan\left(\frac{q_1 q_2 + q_0\, q_3}{0.5 - q_2^2 - q_3^2}\right) \quad \text{(II.19)}$$

II.3.1 Madgwick filter

The Madgwick filter is an attitude and heading reference system (AHRS) algorithm, which is described clearly in (Madgwick, Harrison, & Vaidyanathan, 2011). and (Sarbishei, 2016). It uses the measured acceleration and magnetic field to correct for gyroscopic drift (Admiraal, Wilson & Vaidyanathan, 2017). For the purpose of comparing performances with the proposed method, the Madgwick algorithms and its implementation will be briefly illustrated. This sensor fusion technique is based on two estimates of the orientation: the angular velocity (gyroscope) with its previous orientation estimate and another on gradient descent-based algorithm for orientation estimate respect to gravity. This is a useful tool to fuse the accelerometer, gyroscope, and magnetometer every update step based on the quaternion (Selvarajan & Ananda, 2016), (Xing, et al. 2019), (Brunner, et al, 2015).

Figure II.3 shows the block diagram of the Madgwick filter. Two main processes are used to compute the orientation of the rigid body. First, a correction algorithm is used to align the gyroscope measurements. To minimize the bias and the drift error, both are used to compute the body orientation via the quaternion propagation beginning from the orientation estimated at the previous step. Then, both the accelerometer and magnetometer measurements are fused together using divergence rate β, via the gradient descent algorithm. The output of the gradient descent algorithm is then used to correct the orientation estimated by considering the gyroscope measurements.

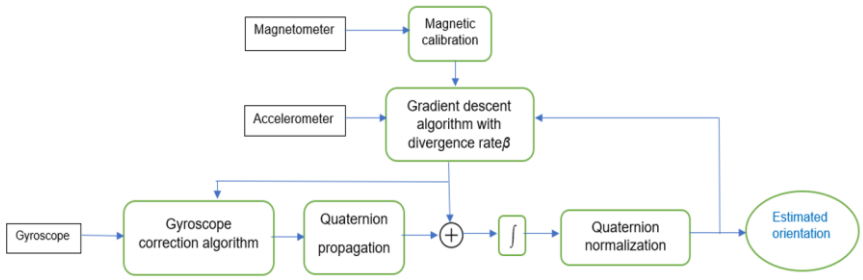

Figure II.3 Madgwick working diagram

The gyroscope measures the angular rate ω_x, ω_y , ω_z (in rads/s), with respect to the x-, y-, and z-axes of the sensor frame, represented in S_ω in the quaternion form.

$$S_\omega = (0\ \omega_x\ \omega_y\ \omega_z) \quad \text{(II.20)}$$

Given ${}^{S}_{E}\hat{q}$ describes the orientation of the Earth frame relative to the Sensor frame in the term of the quaternion, it can be expressed as follows:

$${}^{S}_{E}\hat{q} = (q_0\ q_1\ q_2\ q_3) \quad \text{(II.21)}$$

The quaternion derivative describes the rate of change of orientation of the earth frame relative to the sensor frame ${}^{S}_{E}\dot{q}$ can be calculated as equation II.22.

$${}^{S}_{E}\dot{q} = \frac{1}{2} * {}^{S}_{E}\hat{q} \otimes S_\omega \quad \text{(II.22)}$$

Where the operator $\otimes$ represents quaternion multiplication.

The angular velocity under quaternion form, which shows the Earth frame relative to the sensor frame is called as ${}^{S}_{E}q_{\omega,t}$, the angular rate at time t called as $S_{\omega,t}$ at sampling period Δt.

With ${}^{S}_{E}\hat{q}_{t-1}$ being the previous estimate of orientation:

$${}^{S}_{E}\dot{q}_{\omega,t} = \frac{1}{2}\,{}^{S}_{E}\hat{q}_{t-1} \otimes S_{\omega,t} \quad \text{(II.23)}$$

$${}^{S}_{E}q_{\omega,t} = {}^{S}_{E}\hat{q}_{t-1} + {}^{S}_{E}\dot{q}_{\omega,t}\Delta t \quad \text{(II.24)}$$

The accelerometer and magnetometer reading values are represented in quaternion space as follows:

$S_a = (0, ax , ay, az)$ (II.25)

$S_m = (0, mx, my, mz)$ (II.26)

The Madgwick calculation can be divided into four main steps, described in the following, supposing continuous time t

- Step1: The first step is the calculation of rate of change δq. The variation of the quaternion is calculated using its estimation as follows:

$$\delta q = \frac{1}{2}\dot{q} \otimes S_{\omega} = \frac{1}{2}\begin{pmatrix} -q_1\omega_x - q_2\omega_x - q_3\omega_z \\ q_0\omega_x + q_2\omega_z - q_3\omega_y \\ q_0\omega_y - q_1\omega_z + q_3\omega_x \\ q_0\omega_z + q_1\omega_y - q_2\omega_x \end{pmatrix} \quad \text{(II.27)}$$

- Step 2: A corrective step computation δq based on gradient descent algorithm is performed. Two reference vectors, Ea and Em, respectively, for acceleration and magnetic field, are used to correct the deviation of the algorithm. The acceleration reference vector is defined as follows:

$$Ea = (0, 0, 0, g) \quad \text{(II.28)}$$

Where *g* is the acceleration due to gravity (*g* = 9.8 m/s2). Instead, if there are no magnetic deviations, then the magnetic reference vector E_m can be calculated as described in (NGA & DGC, 2015) and (Ludwig & Burnham, 2018). The correction is calculated due to the Jacobian matrix Jt of the function Ft (Equation II.18) that calculates the error of the projection of rotation on the reference acceleration vector E_a and magnetic reference vector *Em* at time *t* given the acquired value of acceleration *sa,t* and magnetic field $S_{m,t}$

$$Ft = \begin{pmatrix} {}^{S}_{E}q_{t-1}^{-1} \otimes E_{a,t} \otimes {}^{S}_{E}q_{t-1} - S_{a,t} \\ {}^{S}_{E}q_{t-1}^{-1} \otimes E_{m,t} \otimes {}^{S}_{E}q_{t-1} - S_{m,t} \end{pmatrix} \quad \text{(II.29)}$$

$$\delta s = \frac{J_t^T F_T}{\|J_T F_T\|} \quad \text{(II.30)}$$

- *Step 3:* The quaternion change rate *δq* can be corrected with *δs*, calculated in Equation II.19, and integrated as follows:

$$\delta q' = \delta q - \beta \delta s \quad \text{(II.31)}$$

$$q_t = q_{t-1} + \delta q' \Delta t \quad \text{(II.32)}$$

Where $\delta q'$ is the corrected quaternion change rate.

In equation II.20, β is the divergence rate, a parameter that can be defined experimentally. It must be high enough to minimize errors due to integral drift but sufficiently low enough that unnecessary noise is not introduced by large steps of gradient descent iterations.

II.3.2 Mahony filter

The Mahony filter corrects the rotation vector S_ω, based on a Proportional Integral (PI) controller on the correction vector. The error vector is defined as below:

$$e = a \times d \tag{II.33}$$

Where a is the accelerometer vector, d is the gravity vector's direction as given by the estimated attitude.

Generally, the Mahony algorithm is expressed as following steps where Ki and Kp are the integral and proportional adjustable gains.

- Step1: Estimation of gravity vector d from quaternion

$$d = 2\begin{pmatrix} q_1q_3 - q_0q_2 \\ q_0q_1 + q_2q_3 \\ q_0^2 + q_3^2 - \frac{1}{2} \end{pmatrix} \tag{II.34}$$

- Step 2: Calculation of error vector

$$e = a \times d \tag{II.35}$$

- Step 3: Vector integration (I_n) calculation

$$I_n = I_{n-1} + eKi\,\Delta t \tag{II.36}$$

- Step 4: Proportional vector

$$\omega' = \omega + K_p + I_n \tag{II.37}$$

- Step 5: Rate integration of change using $\dot{q} = \frac{1}{2} q \otimes \omega$.

$$q_n = q_{n-1} + \frac{1}{2} q_{n-1} \otimes \omega' \Delta t \tag{II.38}$$

$$= q_{n-1} + \frac{1}{2}\begin{pmatrix} -q_1\omega'_x - q_2\omega'_x - q_3\omega'_z \\ q_0\omega'_x + q_2\omega'_z - q_3\omega'_y \\ q_0\omega'_y - q_1\omega'_z + q_3\omega'_x \\ q_0\omega'_z + q_1\omega'_y - q_2\omega'_x \end{pmatrix}$$

II.4 General comparison

Complementary filter is the simplest algorithm with easy code implementation, but its output suffers more significant noise respect to the others. In contrast, Kalman filter can achieve superior result with lower noise and good dynamic response. However, the complexity of implementation is required with multiple math calculation, included matrix. Madgwick/ Mahony has their advantage via quaternion conversion to avoid the gimbal lock, but it is quite challenging to select the adjusted parameter properly K_p, K_i or the divergence rate to guarantee high performance in term of stability, precision and dynamic behaviour.

Chapter III
'No motion no integration' algorithm

This chapter describes a proposed algorithm NMNI, which optimizes the gyroscope performance by removing drift. As described in the 2 previous chapter, the IMU sensor suffers the big problem with noisy data and yaw measurement challenge. In this chapter, NMNI will be depicted in detail to demonstrate its function on noise minimization and the possibility of yaw calculation without the magnetometer. Moreover, the real-time experiment will show the comparison of acquired angles before and after applying the NMNI to the Madgwick/Mahony filter. The fusion between NMNI and Madgwick filter achieves a significant advantage with higher stability, respects to the traditional Madgwick with magnetometer in heading estimation. Roll and pitch accuracy are also improved thanks to the support of NMNI filter.

III.1 NMNI definition

The NMNI technique is presented with the real-time operation to prevent any single portion of drift when the sensor finishes its motion. The NMNI algorithm is directly applied to the gyroscope to accomplish the highest heading estimation efficiency since no additional noise from other sensors can interfere. A threshold is established based on real gyroscope acquisition at a stationary position to realize the sensor state.
From classical mechanics theory, objects will retain the static state or uniform linear motion until the external force changes this state. Therefore, the stationary state can be reached when the object stops and changes speeds or

direction (Chen, Hu and Sun, 2010). Thus, sensor state detection is the most essential factor for the whole system successfully processed in the proposed model.

Moreover, a threshold update model is added to the NMNI system for long-term performance where the sensor temperature becomes higher, causing an increase in offset in the gyroscope. The principle "No Motion No Integration" and "Renovating Model" construct a real-time operation for the whole system to significantly strengthen the gyroscope characteristic in orientation tracking In order to compensate for bias instability, after the gyroscope is powered on, the MEMS gyroscope is in a stationary position. N samples are collected from the angular velocity bias ω_i and then averaged as the turn-on zero-rate level ω_{bias} to be removed from the next data $\omega[k]$. N number should be enough for calculation, but larger number requires longer time of static state at the initial period. In this case, 100 samples are sufficient. All the subsequent gyroscope readings can then subtract this turn-on zero-rate level as signed integers

$$\omega_{bias} = \sum_{i=0}^{N} \omega_i \qquad \text{(III.1)}$$

$$\omega[k] = \omega[k] - \omega_{bias} \qquad \text{(III. 2)}$$

In the start-up phase, the sensor is in a no-motion state. The abs value of ω is stored with the index of the sample as i (i is an integer number corresponding to the window size), then the filter will keep the highest value $|\omega|$ among these samples as 1st threshold.

$$\omega_{th} = \max \{| \omega [1] |, | |\omega[2] | , \ ... \ | \omega[n] |\} \qquad \text{(III.3)}$$

Where ω_{th} is the first threshold as the boundary between stationary and dynamic conditions.
n is the last index of the window size to select the 1st threshold. Here, n can be selected as 10, which is enough to extract the 1st threshold selection, then it will be updated as described in the next section.

As analysed in chapter I, the gyroscope can be used to calculate the attitude angles yaw, pitch, and roll by integrating the angular rate from the *x*-, *y*-, and *z*-axis measurements ω_x, ω_y and ω_z. The NMNI algorithm calculates the threshold values ω_{xth}, ω_{yth}, and ω_{zth} as the maximum between the absolute value of the acquired samples $\omega_x[i]$,$\omega_y[i]$, and $\omega_z[i]$, based on Equation III.3. These thresholds become the boundary between the static and dynamic conditions. The principle works on the comparison between real-time measured $\omega[k]$ and threshold value ω_{th}.

- $|\omega_x[k]| > \omega_{xth}$ → roll is in rotation; $|\omega_x[k]| \leq \omega_{xth}$ → roll is in static.
- $|\omega_y[k]| > \omega_{yth}$ → pitch is in rotation; $|\omega_y[k]| \leq \omega_{yth}$ → pitch is in static.
- $|\omega_z[k]| > \omega_{zth}$ → yaw is in rotation; $|\omega_z[k]| \leq \omega_{zth}$ → yaw is on static.

Where $\omega_x[k]$, $\omega_y[k]$, $\omega_z[k]$ are the absolute value of current value ω of x-, y-, and z-axis.

The total process of NMNI algorithm is demonstrated in Figure III.1.

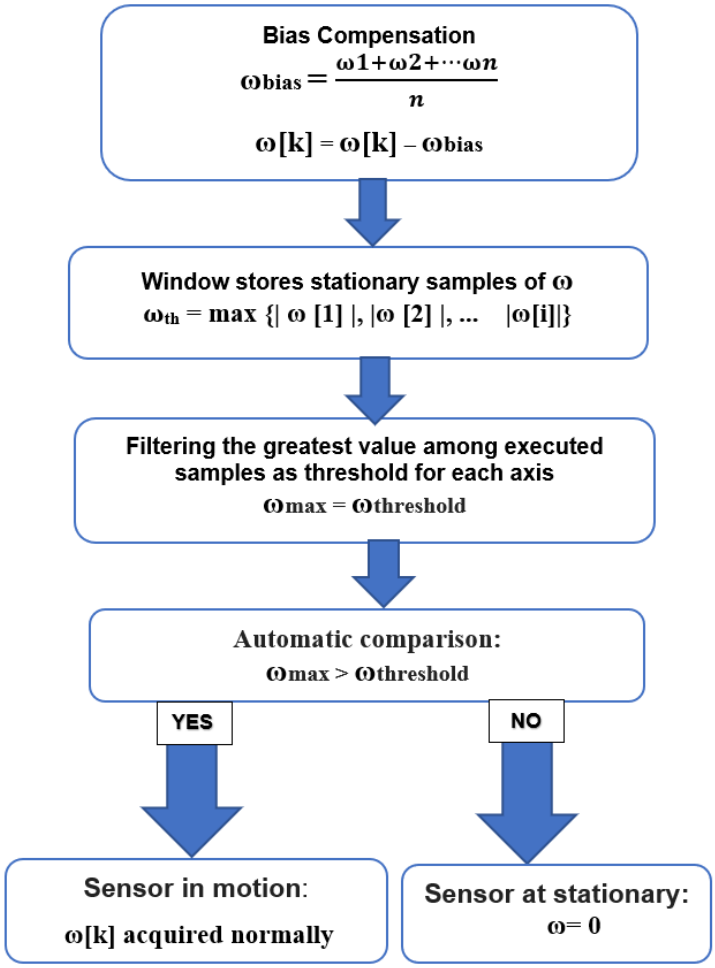

Figure III.1 *NMNI working principle*

III.1.1 NMNI implementation

The implementation of the "NMNI" algorithm can be divided into two parts:
1) The first part is used to calculate sensor offset ω_{bias} like an early mention, which can be seen as an array of N elements with selected number of samples.
2) The second part is aimed to collect ω_{th} and acquisition $|\omega[i]|$ at the current time; this second array has a size of W. These two parts correspond to the parts in which the array structure, stored in memory, is divided. The overall reserved size of the acquisition array will be:

$$\text{Array Size} >= W + N \quad \text{(III.4)}$$

This size must be multiplied by three for the number of axes involved in the calculation. Depending on the desired average time, the array size needs to be extended by the user: the greater the array size for a longer time, the gyroscope has to be stationary. If the array size is too small, the system will be lack data to calculate ω_{th}.

For instance, considering the z-axis, the ω_{zth} value is stored at index 11 of the array, while the 12th element always indicates the current value of ω_{zth}; the same applies for the other axes too. With this technique, the real-time comparison is instituted between $|\omega_z [k]|$ and ω_{zth} .

III.1.2 Threshold Update

To guarantee the system's stability, each time the system is detected to be in a stationary position, a new threshold value is calculated and stored. If the new gyroscope acquisition has an absolute value (abs) higher than the current threshold, it will become the new threshold. This upgrade is necessary for long-term performance when sensor temperature increases, which causes the rise of gyroscope offset. However, to avoid noise, the threshold only updated in the case of difference between abs of angular rate and the current threshold is smaller than the angular rate sensitivity (ARS), which is up to the specifications of each gyroscope. The slowest motion leads to the variation of the least significant bit (LSB) and 1 LSB ≈ ARS. For example, the sensor LSM9DS1 has ARS of 0.00875 °/s which is used as update threshold.
At stationary point (Figure III.2), if $|\omega[k]| > \omega_{th}$ and $|\omega [k]| - \omega_{th} < \text{ARS}$, then $\omega_{th} = |\omega[k]|$.

At this point, the suggested approach appears to incorporate the standard procedure of removing the initial gyro bias (ignoring the Earth rotation) and

an adaptive threshold filter applied to gyroscope measurements before integration that prevents any single drift portion from accumulation.

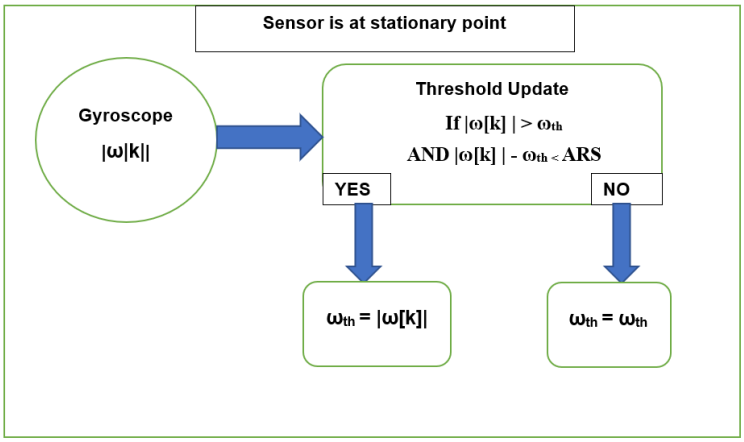

Figure III.2 *NMNI update model*

III.1.3 NMNI Integration with Madgwick or Mahony Filters

The NMNI is a pre-processing technique and can be applied to an attitude and heading reference estimation algorithm, such as Mahony or Madgwick, in order to obtain device or body orientation. As depicted in Figure III.3, before entering the Madgwick or Mahony filter, the gyroscope data pass through the NMNI filter.

1) $|\omega[k]| > \omega_{th}$: The sensor is in motion. ω_x ,ω_y , and ω_z come in the Madgwick or Mahony filter normally.

2) $|\omega[k]| \leq \omega_{th}$: The sensor is stationary. ω_x ,ω_y , and ω_z assume a zero value before entering the desired filter. This fusion technique overcomes the dynamic integration problem on the slope of the NMNI filter and the random drift of the Madgwick or Mahony filter without a magnetometer.

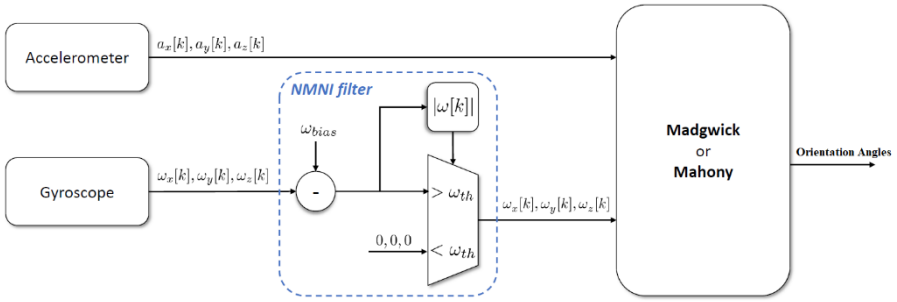

Figure III.3 *Chain diagram of the fusion between Madgwick or Mahony and the NMNI filter*

III.2 Experiments and result analysis

The sensors involved in acquiring data for the experiments are the LSM9DS1 from STMicroelectronics. This device is a system-in-package featuring a tri-axial digital linear acceleration sensor with 16-bit resolution and selectable full-range scale from ±2g to ± 16 g, a 3D digital angular rate sensor with 16-bit resolution and a full range scale of ± 245 degree per second (dps), ± 500 dps and ± 2000 dps the device includes also a 16-bit tri-axial magnetic sensor a magnetic field full scale of ±4, ±8, ±12, ±16 gauss (STMicroelectronics, 2015).

The implementation of the algorithms has been made on an ARM Cortex-M4 based microcontroller STM32F401RE by STMicroelectronics STMicroelectronics, 2015), STMicroelectronics, 2018). This device provides 96 kByte of RAM and 512 kByte of embedded programmable FLASH memory; the clock frequency is up to 84 MHz. The MCU is mounted on its development board ST NUCLEO-F401RE (STMicroelectronics, 2017), (STMicroelectronics, 2018). for easy accessibility to all the required connections.

The sensor is mounted on the STEVAL-MKI159V1 adapter board [44] and connected to the MCU development via an Inter-Integrated Circuit (I2C) communication line of 100 kHz. The output data rate (ODR) of the accelerometer and gyroscope was set at 119 Hz, to achieve a stable transferring signal between the sensor and the computer. Also, the magnetometer ODR is 80 Hz of the period. Hence, the system acquisition is carried out at 119 Hz for the filter without a magnetometer and at 80 Hz vice versa. To guarantee the real time operation, the interrupt was implemented into the MCU, based on the status register of the sensor LSM9DS1. The data

is only acquired when the new IMU data are available by checking the sensor status. The oscilloscope was used to verify the synchronization of data acquisition.

A Pan-Tilt Unit Controller (PTU-C46) (Rollins, R. B. 2000). with a resolution 0.051^0 per position provides fast and accurate positioning of cameras that were manipulated to verify the algorithm performance. The LSM9DS1 mounted on PTU-C for tracking this device orientation. For the evaluation of roll and pitch, the setup is modified and PTU is mounted on the laboratory table vertically as can be seen in Figure III.4. LSM9DS1 sensor assembled on a Printed Circuit Board with the support from long cable to handle the controlled motion comfortably without any restrained problem.

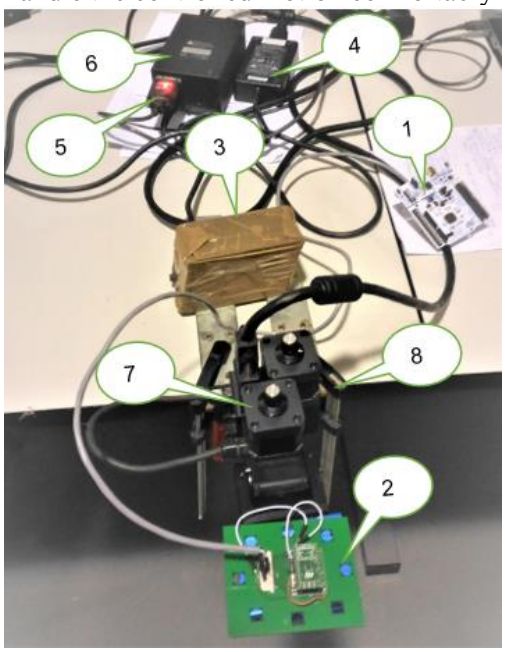

Figure III.4 *Testbench for orientation measurement*

1. NUCLEO-F401RE Board
2. LSM9DS1 Sensor mounted on a Printed Circuit Board
3. Vibrator/Counterweight for balance
4. AC/DC Power Supply
5. RS232 cable
6. PTU-C Controller
7. PTU-C46 Pan Tilt Unit
8. Heavy clamps

After many simulations with adjustable parameters, the best value of each algorithm factor for the experiment was chosen, taken into account the effective compromise among all Euler angles as follows.

- Madgwick: $\beta = 0.40$.
- Mahony: Kp =0.7; Ki = 0.002
- ARS = 0.00875 ^{0}/s

These parameters were selected based on the below approaches:

- β must be high enough to minimize errors due to integral drift but sufficiently low enough that unnecessary noise is not introduced by large steps of gradient descent iterations.
- High value of Kp improves the system response to noise. However, if Kp is too large, the process variable will begin to oscillate, causing unstable control. The integral component sums the error term over time. The result is that even a small error term will cause the integral component to increase slowly. The effect of the integral response is to drive the steady-state error to zero. Small values of Ki are used for the small error term. If Ki is too large, the integral action saturates the controller without the controller driving the error signal toward zero. In the last case, the system will be out of control.
- The sensor LSM9DS1 has ARS of 0.00875 ^{o}/s which is used as update threshold.

III.2.1 Filter behavior analysis and characterization

At the first part, the function of NMNI filter was examined on the yaw measurement, calculated by Madgwick and Mahony without magnetometer. The sensor was kept at a stationary point approximately 0^0 for a minute to observe the drift of the result as well as the potent of the algorithm. Here, the angular rate measurement range is ±245 ^{o}/s.

As shown in Figure III.5, the yaw drift of Madgwick is very fast and when it reached the -180^0, it flips to 180^0 just after less than a minute. Due to the uncontrollable drift, Madgwick algorithm without magnetometer cannot be used for yaw estimation (Madgwick, Harrison & Vaidyanathan, 2011). Therefore, to restraint this drift, the NMNI algorithm is the right solution as the first filter of gyroscope data before arriving Madgwick filter. As a result, the yaw is under control, indicating the appropriate behavior when the sensor is fixed at a position.

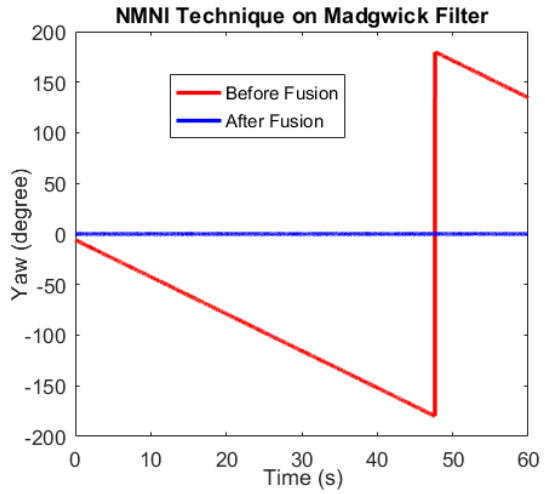

Figure III.5 *NMNI optimization on Madgwick filter*

The Madgwick was improved clearly after the fusion filter; the yaw value is maintained regularly at the stationary point as showed Table III.1. After optimization, the variation is minimized apparently and shows a stable behavior.

Table III.1 *Madgwick static drift analysis.*

Madgwick drift without magnetometer before and after fused with nmni algorithm under static condition		
Yaw drift (°)	Before Fusion (°)	After Fusion (°)
min	5.9	0.010
max	179.9	0.064
mean	39.8	0.041
Std.Dev	50.5	0.007

The same progress carried out as fused Madgwick, the filter fusion with NMNI upgrades the performance of Mahony yaw considerably. As illustrated in Figure III.6, Mahony yaw drifts down approximately 1^0 /s, and it only behaves in the right way after fusion at the static point.

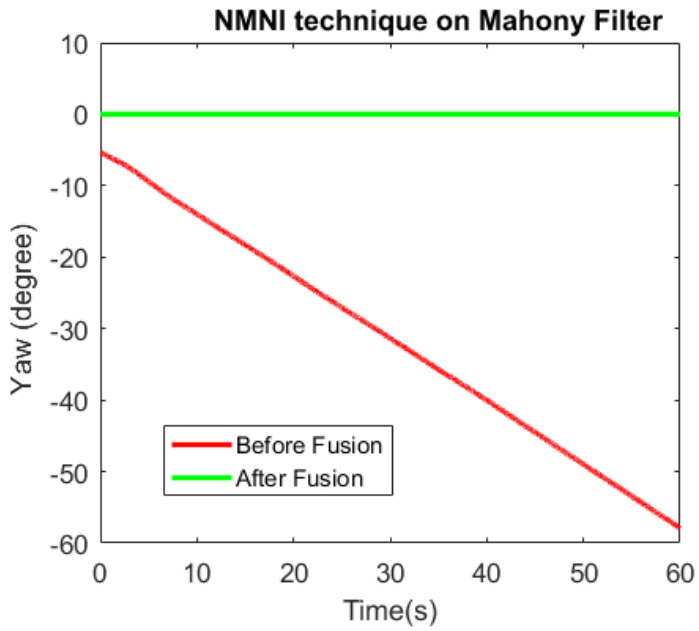

Figure III.6 *Mahony static drift (no magnetometer) before and after fusion.*

Table III.2 *Mahony yaw drift analysis.*

Mahony drift before and after fused with nmni algorithm under static condition		
Yaw drift (°)	Before Fusion (°)	After Fusion (°)
min	5.3	0.170
max	57.9	0.202
mean	31.4	0.175
Std.Dev	15.0	0.031

For the case of fused Madgwick and fused Mahony, the small variation still occurs on heading estimation due to the acceleration components. As observed results from Table III.1 and Table III.2, the NMNI works more effective on the Madgwick filter with less fluctuation of the signal.

Figure III.7 and III.8 show the behavior of roll and pitch before and after applying the NMNI pre-processing technique. The signal is more stable with narrow variation in fused filters. The Fused Mahony filter keeps the signal smoother than the Fused Madgwick filter with an extremely small value of drift.

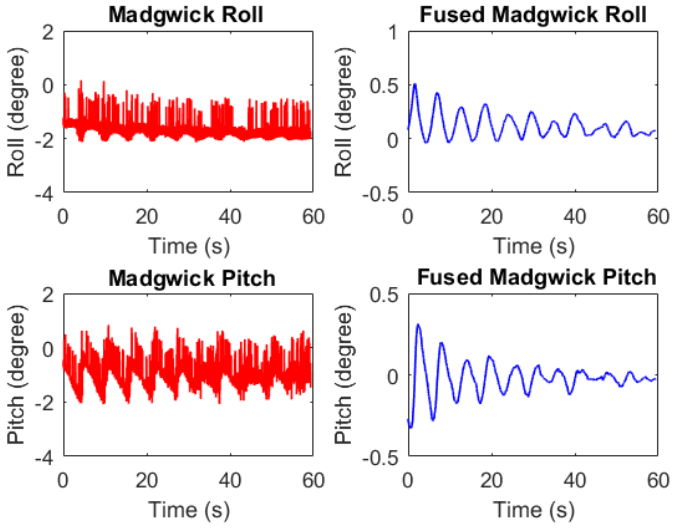

Figure III.7 *Madgwick Roll and Pitch at zero-starting point*

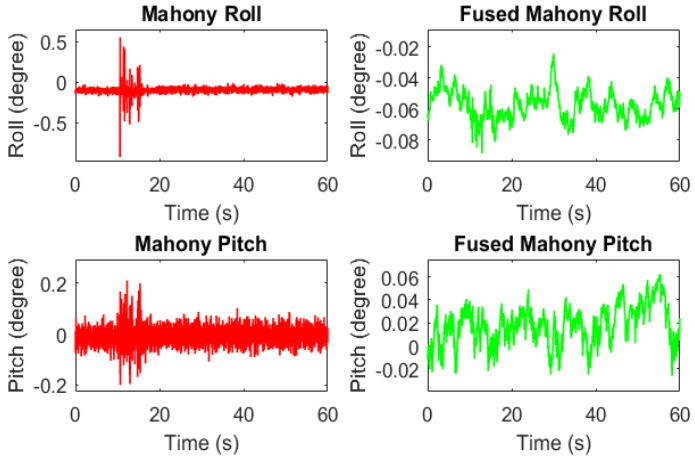

Figure III.8 *Mahony Roll and Pitch at zero-starting point*

The result analysis of roll and pitch are reported in Table III.3 and III.4 Roll is the parameter which is more influenced by drift than pitch in both cases. Thanks to the support of the fusion process, these two Euler angles accomplish optimized drift with Standard Deviation (Std.Dev) only less than 0.11^0 for the Madgwick filter and 0.02^0 for Mahony filter.

Table III.3 *Madgwick roll &pitch drift analysis*

Madgwick roll & pich before and after fused with nmni algorithm under static condition				
Abs Drift Parameters	Madgwick		Fused Madgwick	
	Roll (^{0})	Pitch (^{0})	Roll (^{0})	Pitch (^{0})
min	0.131	0.003	-0.004	0.002
max	2.133	2.073	0.511	0.329
mean	1.681	0.990	0.122	0.068
Std.Dev.	0.302	0.381	0.102	0.071

Table III.4 *Mahony roll &pitch drift analysis*

Mahony roll & pich before and after fused with NMNI algorithm under static condition				
Abs Drift Parameters	Mahony		Fused Mahony	
	Roll (^{0})	Pitch (^{0})	Roll (^{0})	Pitch (^{0})
min	0.002	0.004	0.024	0.003
max	0.923	0.210	0.088	0.062
mean	0.099	0.026	0.057	0.020
Std.Dev.	0.040	0.022	0.009	0.013

III.2.2 Static Test

Yaw is the the main reason why the magnetometer must be used in the 9 Degree of Freedom (DoF) platform. As mentioned in chapter I, this sensor increases the complexity of the system due to complicated calibration process, and also the concern of vulnerability to the iron distortion.
Thus, the 1st test is about the comparison between the Madgwick with magnetometer and Fused Madgwick, included NMNI algorithm without magnetometer.

To observe the pros and cons of a new algorithm, PTUC was controlled to move from 0° to 90° with a different step at 30°, 100 samples were extracted from each angle to analyze the behaviour of the algorithms. Generally, a larger angle conducts larger error as result in Table III.5. Both Fused Madgwick and magnetic Madgwick show convincing achievement. The filter fusion accomplishes smaller error at 30° and 90° and slightly higher at 60°. Figure III.9 shows that the fused Madgwick estimates smoother value while the Madgwick in presence of magnetic sensor generates larger variation during the test with smaller Std.Dev. For the case of 90°, the Madgwick generates a transient before reaching the proper angle.

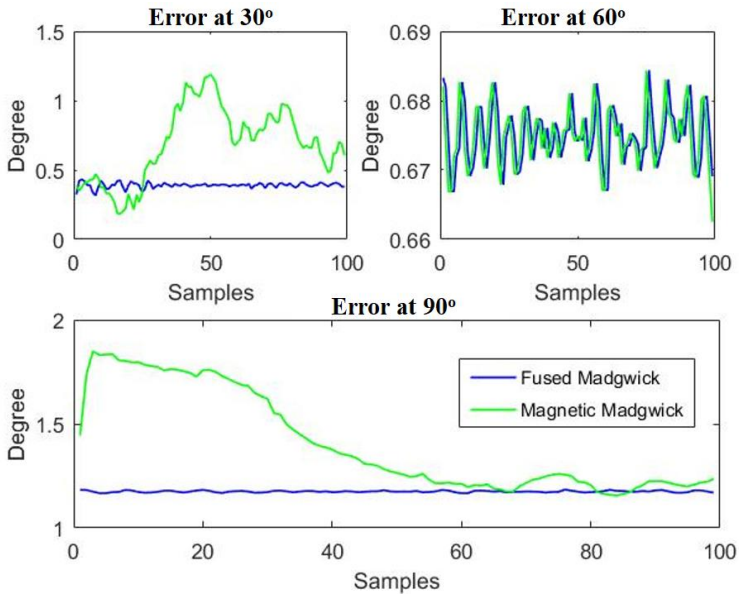

Figure III.9 *Error at different heading angles compared with the reference*

Table III.5 *Heading calculation under static condition*

PTU-C Angle (°)	Madgwick with magnetometer		Fused Madgwick	
	Mean (°)	Std.Dev. (°)	Mean (°)	Std.Dev. (°)
30	30.564	0.36	30.39	0.12
60	60.670	0.021	60.673	0.011
90	91.45	0.24	91.120	0.020

Figure III.10 shows the good performance of both Fused Madgiwck and Fused Mahony when the reference angle of roll, pitch and yaw stay at 50°.

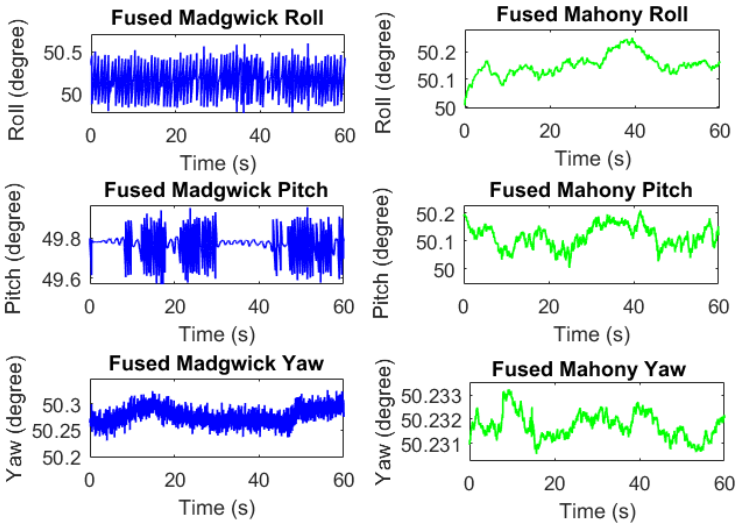

Figure III.10 *Euler angles tracking at 50 degree*

III.2.3 Dynamic Test

For the test of the dynamic test, the device PTU-C was moved from 0^0 to 90^0 back and forth for 40 s. Each time the PTU-C reaches the edged points: 0^0 or 90^0, this device is in stillness in an extremely short period of time due to inertia which is the resistance of a physical object to change in its direction of motion. This period is very critical because even just a small drift portion occurs at this moment, the errors would accumulate and yield the incorrect

measurement. Therefore, the NMNI filter must be exact to eliminate these drift portions.

The PTU-C rotates ten turns back and forth at velocity 45^0/s as demonstrated in Figure III.11. Mean value and Std.Dev are reported for data evaluation in Table III.6.

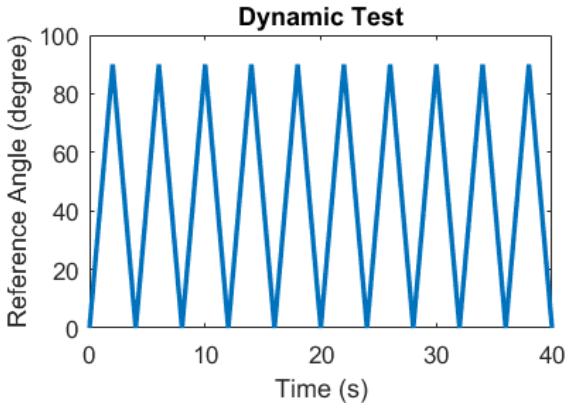

Figure III.11 *Test reference for dynamic case.*

Under this stressful test, the Fused Madgwick filter accomplishes more stable result than Fused Mahony filter with less variation between 10 cycles. Both 2 filters suffer more significant error at 90° than 0° with mean value is more far away than true value. The Std.Dev of Yaw is higher than roll and pitch since the roll and pitch still can get the major support of accelerometer, while the yaw measurement mainly relies on the NMNI optimization with gyroscope. Generally, the Fused Mahony conducts more error at heading estimation, but it still shows its potential accuracy in orientation tracking

Table III.6 *Reported result of dynamic test*

Euler Angle (°)		Fused Madgwick		Fused Mahony	
		Mean (°)	Std.Dev (°)	Mean (°)	Std.Dev (°)
Roll	0	0.205	0.020	0.201	0.019
	90	90.341	0.047	90.305	0.048
Pitch	0	0.194	0.031	0.253	0.031
	90	90.287	0.108	90.35	0.154

Yaw	0	0.281	0.235	0.316	0.322
	90	90.780	0.304	90.983	0.350

III.2.4 Temperature Behavior

To observe the behaviour of the orientation angles during the temperature variation, a smart experiment was carried out on the earth frame. The temperature of the sensor was increased in the range of 25 ºC to 40 ºC with the help of heat air flux. The temperature was measured with the embedded temperature sensor in the LSM9DS1 module. For each temperature step, 50 samples were extracted for the mean value calculation.
As shown in Figure III.13, the orientation values of the fused Mahony filter and the fused Madgiwck filter have high stability under the temperature change. The maximum fluctuation of the fused Madgwick filter is only about 0.080^0 at 40ºC. On the other hand, the Mahony filter demonstrates better immunity in temperature variation with smaller alterations in all Euler angles.

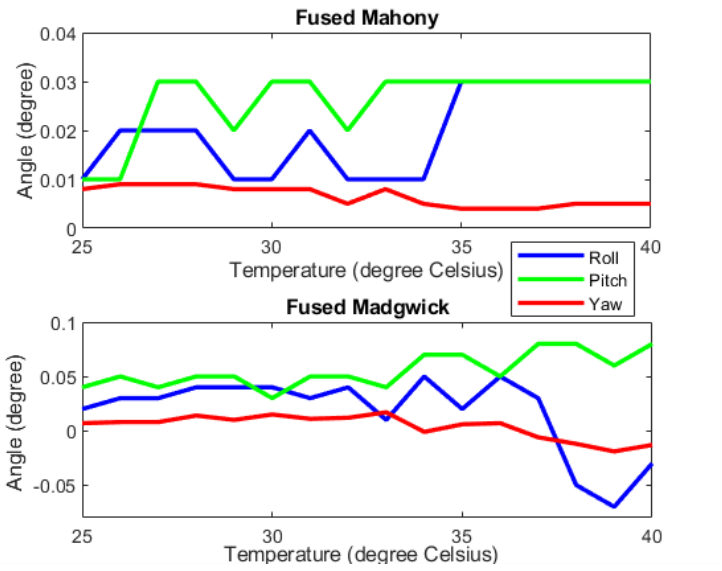

Figure III.12 *Temperature variation test*

III.3 NMNI method conclusion

In this chapter, the development of a filter algorithm with the optimization of the NMNI technique is reported. The experimental results verify the significant improvement of the Mahony and Madgwick filters in orientation tracking due to the proposed pre-processing model. The fused Madgwick is strongly recommended for heading and yaw estimation, while the fused Mahony can track roll and pitch at closer reference angles with less drift and high precision. The real-time measurement has been completed so far via tests of static–dynamic-mixed motion. Both filters, when fused with the NMNI technique, have a good command of detecting the inclination and heading with narrow errors and high stability during operation. The variation due to temperature is kept at the minimum level. The NMNI technique is a promising collaborator with other sensor fusions methods via effectiveness maximization for the gyroscope.

Chapter IV
OACP algorithm on vibration optimization of industrial inclinometer for MEMS accelerometer

As previously reported in chapter II and chapter III, the sensor fusion algorithms were demonstrated as well as their characteristics and working principle in the noise disturbance. Chapter IV presents a new algorithm Orientation Axes Crossover Processing (OACP) (Hoang & Pietrosanto, 2021) on vibration optimization for MEMS accelerometer without sensor fusion. In industry, inclinometer suffers high external impact from vibration that reduces its precision. For example, when inclinometer is mounted on the excavator chassis to measure the horizontal inclination of the body and transmit the data to the control system. By detecting this angle, the operator properly judges the actual magnitude of the digging force at that angle to prevent the excessive digging force and leading forward. This process ensures the machine is working at a safe grade to prevent rollover. However, the excavator generates the considerable vibration which negatively impacts the inclination precision that can cause the wrong angle output. Thus, the OACP is designed to optimally minimize these significant noises based on the characteristics of vibration impact on whether the X-axis or Y-axis. The aim is to optimize the inclination with solely accelerometer without other sensors support.

IV.1 Low-pass filter

Before introducing the OACP algorithm, a LP filter is described in detail because this type of filter is popularly applied to accelerometer for noise minimization. LP filter removes high-frequency noise by allowing only low-

frequency signals to pass through, as demonstrated in Figure IV.1. In this system, a simple but effective LP filter is designed based on the below algorithm.

$$Y = (\alpha) * (y_{t-1}) + (1 - \alpha) * (y_t) \quad (IV.1)$$

Where: α is the filter coefficient; y_t and y_{t-1} are output acceleration at the current sample and the previous sample respectively; Y is the filtered acceleration.

The filter coefficient can be evaluated based on the time period (τ) of the desired cut-off frequency (fcut) and loop time (dt) of the accelerometer output data rate.

$$\tau = \frac{1}{f_{cut}} \quad (IV.2)$$

$$\alpha = \frac{\tau}{\tau + dt} \quad (IV.3)$$

Where the acquisition value from accelerometers are Xacc and Yacc as the inputs of the LP filter and X and Y defined as outputs acceleration.

Figure IV.1 *Chart of LP filter*

IV.2 OACP filter

The OACP works on the vibration impact's characteristics, whether X-axis or Y-axis. If vibration mainly occurs on X-axis, the roll will suffer considerable variation while pitch gets small change. Therefore, the OACP filter sets up a suitable threshold based on two consecutive samples of Y-axis acceleration (Yacc) to whether the Xaxis acceleration (Xacc) is used for roll calculation or not and vice versa for pitch evaluation. The "Axes Crossover" principle is processed by using a threshold of acceleration variation on the X-axis (ΔXacc) to optimize the Y angle and threshold of acceleration variation on the Y-axis (ΔYacc) to optimize X angle. This threshold is updated practically, based on vibration characteristics.

The OACP filter is able to fuse with other filters such as the LP filter and the Kalman filter:

- The filter fusion is the combination of LP filter and OACP filters
- Kalman_acc filter is named for the implementation of the OACP technique into the Kalman filter. This method requires only the accelerometer to enhance its dynamic response without gyroscope support.

On the other hand, the vibration impacts are taken into account for both static and dynamic cases. The static case is analysed when the sensor is on the Earth frame; no dynamic motion is applied. The dynamic test shows how each kind of filter handles the fluctuation of the external noise during the motion and how fast they achieve a stable result when the dynamic motion ends.

IV.2.1 Operating principle

Practically, the vibration can strongly influence on X-axis or Y-axis for a specified time. The OACP filter works on the difference between absolute values of 2 consecutive acceleration samples of each axis ΔX, ΔY.

$$\Delta X = abs(|X_n| - |X_{n-1}|) \quad (IV.4)$$

$$\Delta Y = abs(| Y_n| - | Y_{n-1}|) \quad (IV.5)$$

Where n is the index of the current sample; X and Y are the filtered acceleration from the LP filter.

Not only during vibration but also the dynamic inclination of the X-axis (roll), ΔY has a small variation in mg while ΔX has significant value.
Similarly, when vibration occurs on Y-axis or while pitch rotates, ΔX has a slight variation, in contrast to the high value of ΔY.

According to orientation formula in Equation (I.1) and Equation (I.2), roll measurement requires good immunity to vibration on the X-axis for the Xacc. Pitch measurement needs high vibration immunity for Yacc. A threshold is set as the boundary for vibration and the axis motion of inclination. The OACP filter works on the threshold of the axis, which has the lowest variation value in each vibration case. This function is straightforward and highly effective for vibration characteristics.

ΔX threshold, ΔY threshold are selected with narrow but suitable value to detect whether the vibration or the motion occurs. During the vibration, the variation when sensor stays at static is smaller than during dynamic motion.
As illustrated in Figure IV.2:

- If the vibration on X-axis and motion occurs on the roll, ΔY get the least variation → OACP filter has the primary role in optimizing the

vibration impact on roll (a strong variety on Xacc) by using ΔY threshold condition.

- If the vibration on Y-axis and motion occurs on the pitch, ΔX get the lowest variation → OACP filter has the main role in optimizing the vibration impact on the pitch (a strong change on Yacc), by using ΔX threshold condition.

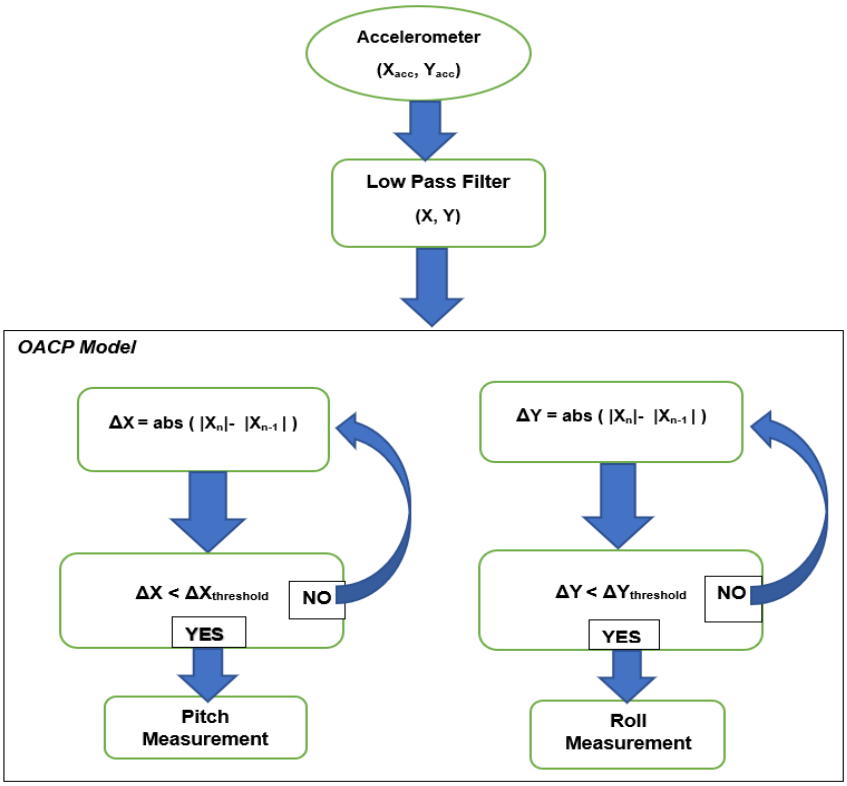

Figure IV. 2 *OACP filter diagram*

Once the energetic vibration occurs on the sensor, both X-axis and Y-axis suffer the variation. However, the amplitude of variation is the difference between ΔX and ΔY, depends on whether vibration mainly impacts right-left (X-axis) or forward-backward (Y-axis).

Vibration mainly befalls on Y-axis:

- Pitch needs to be filtered adequately.

➔ X varies less than ΔY and has a better stability.

➔ The threshold on X-axis is selected because now, ΔY has a significant variation → ΔY threshold must be big and more difficult to collect.

➔ Since vibrations cause ΔX to vary under ΔX threshold, no noise calculation can be accumulated in pitch.

In that way, the same principle is carried out when vibration on X-axis. X threshold is collected to prevent noise from the roll.

If ΔX < ΔX threshold → pitch calculation

If ΔY < ΔY threshold → roll calculation

IV.2.2 Threshold update

To be practical, the threshold must be updated which depends on the vibration characteristic. After numerous tests, the starting threshold is supposed to be 1mg. This value is suitable since the crossing threshold is chosen, based on the axis variation when the vibration does not occur directly like a detailed analysis in the previous part. Here, Δacc is the absolute variation value between 2 acceleration samples. Δth is the threshold value of Δacc.

During mechanical operation, vibrations happen fast with high frequency. Two counters set up:

- Counter_up: When stronger vibration causes a more significant value of Δacc, so Δth increases.
- Counter_down: When weaker vibrations cause less variation on acceleration, so the threshold decreases.

An update resolution is an input for the model. The Δth changes by adding or subtracting this value. More significant resolution faster updates but it can exceed the proper value. In contrast, a smaller resolution will update slower but more precise. This working concept is based on gradient descent principle (Jaber and Frye, 2020). According to the theory of Nyquist frequency, the input frequency should be less than half of the sampling rate of the concerned signal. If Δacc of multiple vibrations continuously differ from Δth, it means that this Δth must be adjusted to follow the current situation of vibration. The Δth is updated when vibrations cause acc different to Δth with frequency more than Output Data Rate (ODR)/3 for a second. The updated model is described as Table IV.1, with an update resolution is 0.2mg.

Table IV.1 *Threshold Update Model*

Vibration Changes	Update Procedures
Stronger	. If (Δacc > Δth): {counter_up +=1}; . For 1 second, if (counter_up ≥ ODR/3) { Δth += 0.2}
Weaker	. If (Δacc < Δth): {counter_down +=1}; . For 1 second, if (counter_down ≥ ODR/3) { Δth − = 0.2}

At this point, the threshold is updated in real-time and enhances the precision of the OACP for inclination measurement.

IV.2.2 Combination between Kalman filter and OACP filter

Kalman filter is the powerful filter which effectively works on noise as discussed early in chapter II.

- For the traditional method, the orientation angles are calculated from the LP filter data, then fuse with the angular rate (ω_x, ω_y) as in Figure IV.3.
- For the case of combination between Kalman and OACP filter, the OACP data, is directly fused with the inclination data from the LP filter, as IV.5. This fusion technique generates Kalman outputs (Roll_Kalman_acc and Pitch_Kalman_acc), which require only accelerations as inputs.

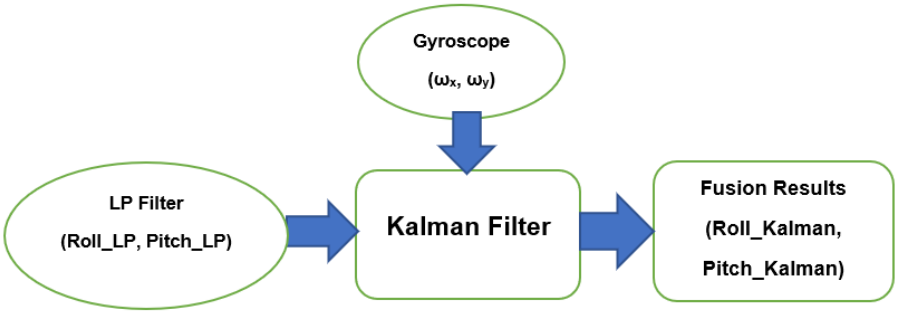

Figure IV.3 *Chart of Kalman filter (sensor fusion)*

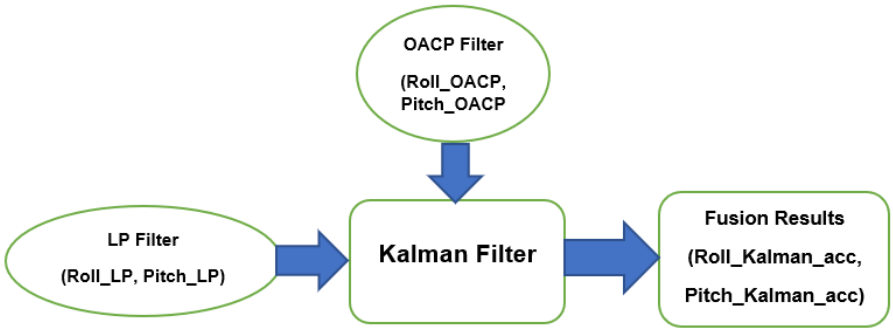

Figure IV.4 *Chart of Kalman_acc filter*

IV.2.3 Fusion filter

Like the Kalman_acc filter, the Fusion filter combines 2 filters: OACP filter and LP filter. The inclination measurement from the acceleration of the LP filter contains the fast- dynamic response, which is fused with the high vibration immunity data from the OACP filter as an improved version of the OACP algorithm in Figure IV.5

$$\text{Roll\_fusion} = \beta * \text{Roll\_OACP} + (1 - \beta) * \text{Roll\_LP} \quad (\text{IV.6})$$

$$\text{Pitch\_fusion} = \beta * \text{Pitch\_OACP} + (1 - \beta) * \text{Pitch\_LP} \quad (\text{IV.7})$$

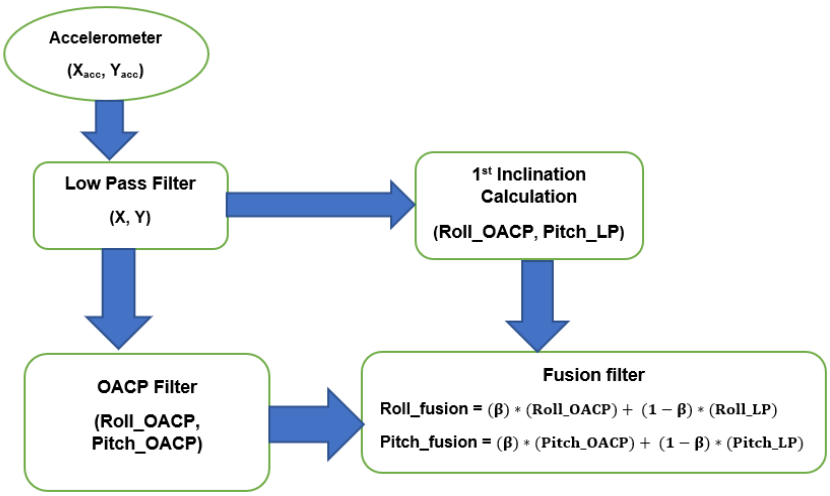

Figure IV.5 *Fusion filter diagram*

IV.3 Experimental analysis

With the same test bench as NMNI test (Figure III.4), the OACP algorithm was examined in both static and dynamic case. The ODR of accelerometer and gyroscope were set to 119 Hz. The gyroscope data were only used in the traditional Kalman filter.
After multiple tests, the best value of adjustable parameters for each algorithm were chosen to obtain the optimized performances as follows:

- LP coefficient: $\alpha = 0.9$
- Kalman parameters: Qbias = 0.1, Qacc = 0.05, R =0.0006.
- Fusion Filter coefficient: $\beta = 0.2$
- Starting threshold: $\Delta X_{threshold} = \Delta Y_{threshold} = 1mg$

These parameters were chosen, depending on the following characteristics:

- The LP filter coefficient was chosen to remove the noise effectively but still guarantees the dynamic response, also with the concern of Nyquist theory.
- The Kalman uncertainties were selected based on the description of Kalman filter in section II.2 of chapter II.
- The Fusion Filter coefficient should be in a compromise between the OACP filter and LP filter. Higher β leads the signal more like the OACP output (better in noise removal). Smaller β provides more

characteristics of LP filter for the signal (faster dynamic response). With β = 0.2, the signal removes the noise effectively with a better dynamic response.

- The starting threshold is significant enough based on the OACP working principle. Moreover, this value can be updated automatically during operation.

IV.3.1 LP filter verification

To guarantee the efficiency of the LP filter, a quick experiment is carried out. The sensor is horizontally placed on the vibrator for 1 minute, and then the result is reported in Table IV.2 to verify the performance of the LP filter. As shown in IV.6 the LP filter significantly reduces noise from raw measurement that confirms the success of LP filter design in noise removal.

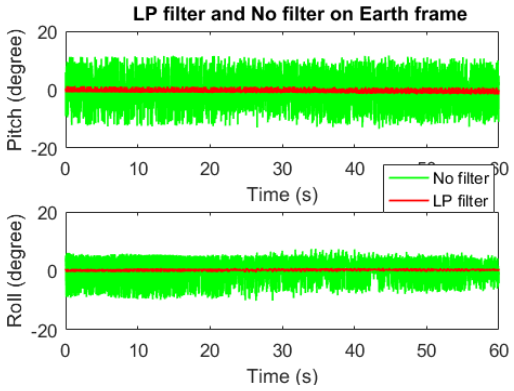

Figure IV.6 *Noise reduction by LP filter*

Table IV.2 *Reported data: before and after LP filter*

Variation Absolute value parameters	No filter	LP filter
Pitch mean (^{0})	5.184	0.654
Pitch max (^{0})	13.424	1.701
Pitch Std (^{0})	3.518	0.391

The maximum spike decreases from more than 10^0 to less than 1.8^0 for both roll and pitch. Mean and standard deviation (std) values are minimized noticeably.

IV.3.2 Inclination test

After LP filter test, since now the robust test bench (Figure III.4) is utilized for experiment. Different from the previous test, the sensor is mounted on the PTU-C controller, so the vibration is more robust due to the interaction between the vibrator and mechanical parts of the device. All the algorithms are processed based on this system to see the difference in each filter

To analyze the behavior of the OACP filter on inclination, roll, and pitch were controlled to tilt alternately at 15^0, $30^{0,}$ and 45^0 for 30 s. This test characterized how the LP filter change after OACP optimization on inclination.

Figure IV.7 shows the signal of the LP filter before and after the OACP process on a slope of 30^0. The LP performance is improved thanks to the optimization of the OACP technique significantly. The spikes are restrained clearly, and the acquired signal becomes more stable with less variation.

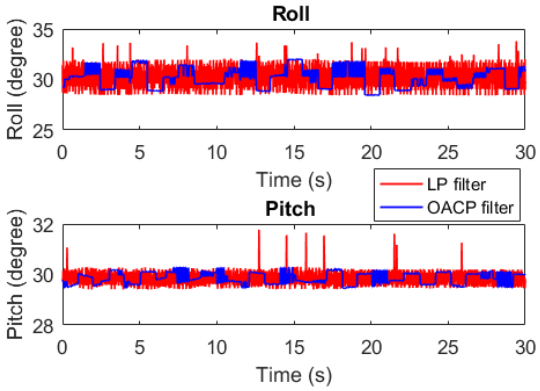

Figure IV.7 *LP and OACP on slope of 30 degree*

As reported in Table IV.3, vibration conducts in roll more seriously than pitch since roll std is more significant than pitch std. For this case, roll data suffer more considerable variation. On the other hand, the OACP adapts well with various inclinations where the spikes as well as vibrated behavior, always minor apparently. Besides, the mean value of orientation position is maintained closer to the reference by the OACP technique, respect to LP filter.

Table IV.3 *Vibration impact on the inclinations*

	Oriental Reference					
	LP filter			After OACP filter		
Reference (°)	15	30	45	15	30	45
Roll mean (°)	15.42	30.29	45.5	15.07	30.24	45.44
Roll most significant spike (°)	3.12	3.79	2.03	1.35	1.80	0.89
Roll std (°)	0.69	1.07	0.54	0.59	0.80	0.33
Pitch mean (°)	15.06	29.5	44.2	15.3	29.94	44.55
Pitch most significant spike (°)	1.53	1.77	2.15	0.44	0.30	0.23
Pitch std (°)	0.19	0.27	0.33	0.17	0.22	0.32

IV.3.2 Filter Comparison

In this part, there are 2 main tests:

- For the static test, the sensor is kept on the Earth frame, which does not incline for 60 seconds to observe how the vibration impact on each filter.
- For the dynamic test, the pitch is rotated from 10° to 60°, then the roll is rotated from -10° to 30° about ten cycles for each test. There are short periods of static position between peak to peak and cycle to cycle. The characteristics of the filter behaviour are inspected via the way each algorithm reacts to vibration and also time response to dynamic motion

Static Test:

- LP filter vs. OACP filter

Like the previous test, the OACP filter is applied to the LP filter to observe the optimization of the proposed method. As shown in Figure IV.8, the OACP filter restrains the strange spikes of inclination measurement. This improvement is advantageous to keep the right result from sudden change caused by vibration.

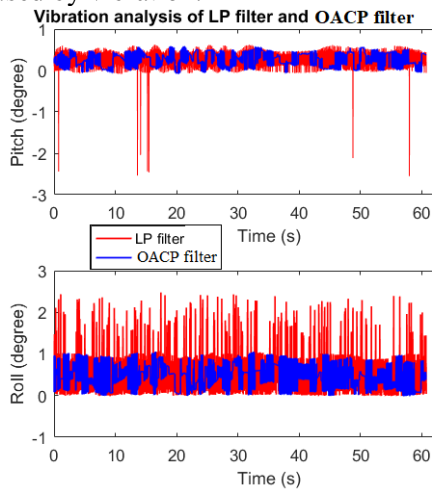

Figure IV.8 *LP filter and OACP filter on Earth frame*

- OACP vs. Fusion filter characteristic

In this part, the processing behaviours of the OACP filter and Fusion filter are evaluated to observe the pros and cons of each type of filter. The acquisition value of the Fusion filter varies back and forth more closely to 0 than the OACP filter, as shown in Figure IV.9 and Figure IV.10. The OACP filter is less vulnerable to the vibratory influence. However, once it is affected, the signal remains at the fluctuated value for longer than what happened with the fusion filter. Therefore, the mean value of the OACP filter is higher than the Fusion filter, as reported in Table IV.4.

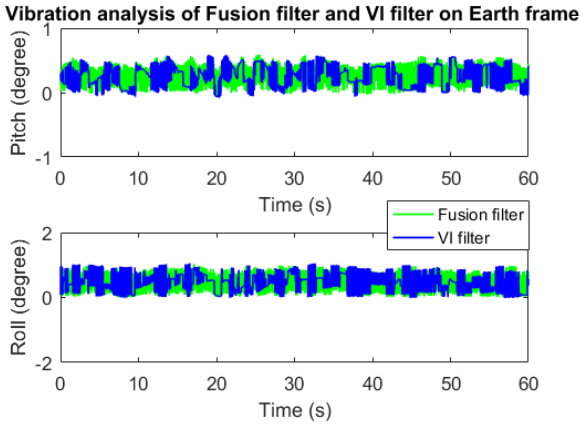

Figure IV.9 *Fusion filter and OACP filter on Earth frame*

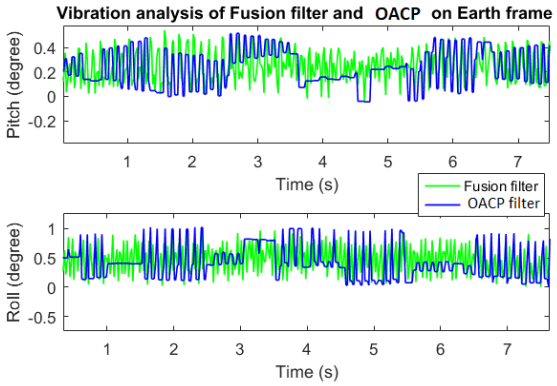

Figure IV.10 *Behavior of Fusion filter and OACP filter*

Table IV.4 *The vibration impact on filters*

Absolute Variation parameter	LP filter	OACP filter	Fusion Filter	Kalman filter (Sensor fusion)	Kalman_acc
Pitch mean	0.26^0	0.25^0	0.25^0	0.25^0	0.25^0
Pitch max	2.55^0	0.58^0	0.59^0	0.61^0	0.62^0
Pitch Std	0.19^0	0.17^0	0.14^0	0.16^0	0.16^0
Roll mean	0.55^0	0.40^0	0.46^0	0.47^0	0.46^0
Roll max	2.47^0	1.05^0	1.05^0	1.06^0	1.05^0
Roll Std	0.43^0	0.27^0	0.26^0	0.30^0	0.30^0

- Filter fusion vs. Kalman filter vs. Kalman_acc filter

The Fusion filter behaves quite similarly to the Kalman filter. Meanwhile, the Kalman filter and Kalman_acc filter are nearly the same with a minimal variation, like Figure IV.11 and Figure IV.12.

Table IV.4 reports data of all algorithms during vibration impact for 60 s. The LP filter has an enormous variation caused by vibration. The OACP filter and Fusion filter achieve the best performance in the term of vibration immunity. Meanwhile, 2 Kalman filters are competitive with each other, with a slight difference only.

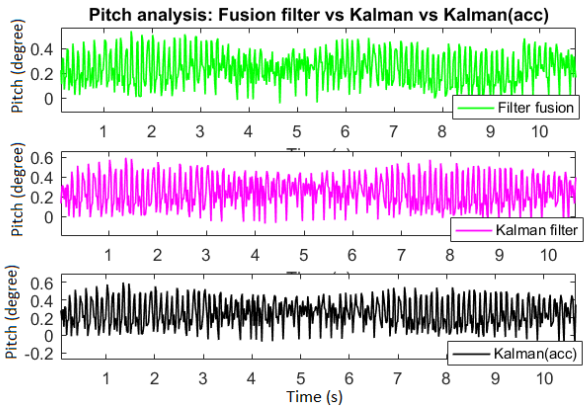

Figure IV.11 *Pitch of Filter fusion vs. Kalman filter vs. Kalman_acc filter on Earth frame*

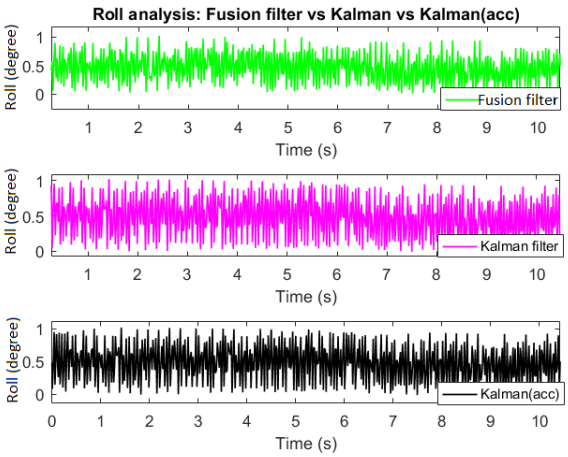

Figure IV.12 *Roll of Filter fusion vs. Kalman filter vs. Kalman_acc filter on Earth frame*

Dynamic test

In the dynamic experiment, the dynamic behavior and time response of each filter is evaluated appropriately. Each time, the PTU-C finishes its motion, it rests at a static position for a short time to observe the inclination.

- Pitch dynamic rotation

The roll is controlled to rotate from 10° to 60°. Here, the LP filter is red line, OACP filter is blue line, and Fusion filter is green line.

LP, OACP, and Fusion filter - as seen in the dynamic behavior of pitch in Figure IV.13 and Figure IV.14, the OACP filter reaches the static value by step movement. Unlike LP and Fusion filter, the OACP filter has the trend to calculate the value directly when the sensor ends its rotation. Although the OACP filter has more stable at static situation, sometimes it gets a small delay compared with the LP filter. This feature is improved in the Fusion filter with better dynamic behavior with the combination of the noise removal of the OACP filter and the fast-dynamic response of the LP filter.

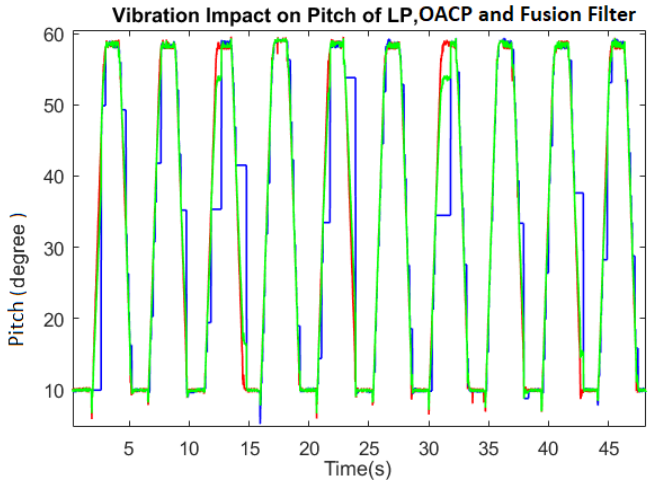

Figure IV.13 *LP, OACP, Fusion filter dynamic motion*

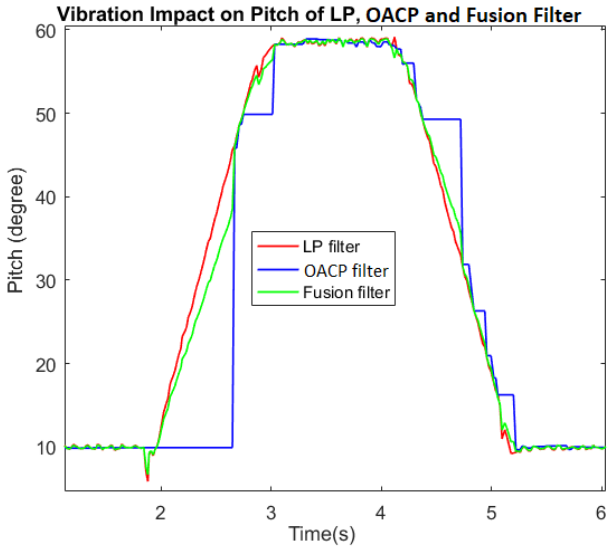

Figure IV.14 *Pitch of LP, OACP and Fusion filter behavior*

As shown in Figure IV.15, the behavior of the Kalman filter and Kalman_acc filter are close to each other. They have a good dynamic response and make the signal smoother, with respect to the LP filter. Related to the static parameters, the Kalman filters remove the noise effectively without significant spike.

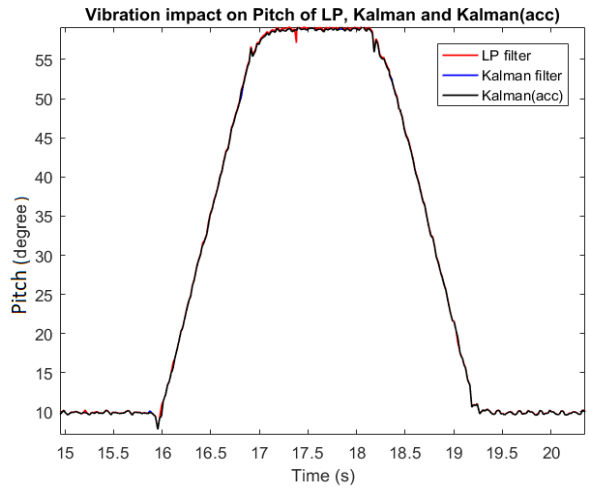

Figure IV.15 *Pitch of LP and 2 Kalman filters behavior*

- Roll dynamic rotation

The roll is controlled to rotate from -10° to 30°. As mentioned above, the OACP filter can generate delays occasionally. However, it is more stable for the static parameter, as shown in Figure IV.16. The Fusion filter does not have strange spikes like the LP filter and accomplishes the last value nearly at the same time with the LP filter.

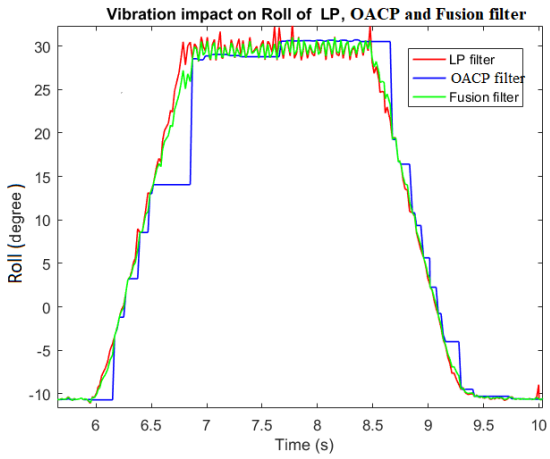

Figure IV.16 *Roll of LP, OACP and Fusion filter behavior*

Similar to the pitch case, both two Kalman filers achieves less variation than LP filter as Figure IV.17. Despite the corresponding performance, a significant advantage of Kalman_acc filter is the processing operation with the absence of gyroscope

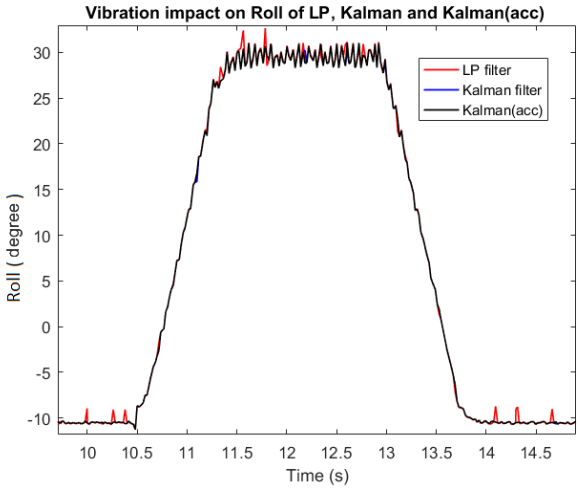

Figure IV.17 *Roll of LP and 2 Kalman filters behavior*

IV.3.3 Dynamic time response

Practically, the user wants to receive the inclination measurement as fast as possible when the sensor is stopped its motion. Therefore, two important parameters should be considered:

- Time_rise: from the starting time of motion from low to high until staying at a maximum stable value.
- Time_down: from the starting time of motion from high to low until staying at a minimum stable value.

The rotating speed of PTU-C is 50^0/second. To make the comparison in terms of dynamic time, the mean time value of 10 cycles is calculated from the above dynamic motion: pitch (10^0 to 60^0), roll (-10^0 to 30^0), as shown in Table IV.5 and Table IV.6. All the units are reported in second, and the dynamic motion always suffers the vibration impact. The reference time of the dynamic pitch, dynamic roll are 1s and 0.8 s respectively for each Time_rise or Time_down

Table IV.5 *Dynamic mean time of pitch (10 cycles)*

Dynamic time	LP filter	OACP filter	Fusion filter	Kalman filter	Kal_acc filter
Time_rise (s)	1.030	1.171	1.171	1.036	1.030
Time_down (s)	1.157	1.425	1.223	1.163	1.163

Table IV.6 *Dynamic mean time of roll (10 cycles)*

Dynamic time	LP filter	OACP filter	Fusion filter	Kalman filter	Kal_acc filter
Time_rise (s)	0.808	0.853	0.812	0.808	0.808
Time_down (s)	0.827	0.888	0.848	0.827	0.827

Generally, all the filters performed a good dynamic response,compared with time reference. The small delay values can be understood by the vibration impact. During the dynamic rotation, Time_rise is faster than Time_down.

The reported data from Table IV.5 and Table IV.6 indicate that the dynamic time of the LP filter and 2 Kalman filters are close to each other. The sensor fusion Kalman is slower than Kalman_acc filter only in Time_rise of the pitch. The dynamic time of the OACP filter is improved in the Fusion filter but still requires a longer time to attain the stable value, respected to Kalman filters.

IV.4 OACP algorithm conclusion

This work has introduced a new algorithm with the practical principle to optimize the vibration impact based on the MEMS accelerometer with the absence of other sensors. The inclinational measurements were analyzed in detail for static and dynamic cases. The OACP filter can work independently and remove the considerable spikes from the LP filter. Furthermore, its dynamic performance in terms of time is apparently improved by fusing with the LP filter and Kalman algorithm. The Kalman_acc filter shows a highly competitive accomplishment with the traditional Kalman filter, which requires gyroscope support. This research relief the burden on the LP filter and also solves the economic problem in the industrial inclinometer in dealing with the external noise without sensor fusion.

Chapter V
Robust orientation system for inclinometer with full redundancy in heavy industry

This chapter describes an orientation structure for industrial inclinometer based on MEMS accelerometer. An industrial motor (Vexta) is used as an oriental reference. The STM microcontroller (MCU) has the role of recording the inclination sent from the motor with the corresponding acceleration into a Lookup Table (LUT) by using Flash memory (Hoang et al., 2020). The full redundancy included dual accelerometers and MCUs to enhance the safety function for the operating system via two inclination channels. The support from the LP filter and the zero-offset compensation for temperature change contribute to the measurement precision. For industrial applications, Control Area Network open (CANopen) is used as an embedded network communication system. Both static and dynamic cases were tested to verify the behavior of the inclination sensor. The designed structure provides high efficiency for inclinometer performance with accuracy ±0.2° and the stability is always guaranteed thanks to safety function. The designed inclinometer was used for a real excavator to verify its stability and operating performance. The project was carried out at the 'Sensor System' in Italy, an industrial company in the inclinometer field.

V.1 System overview

The inclinometer is calibrated based on the oriental motor as a reference, the accelerations and corresponding angles are memorized in Flash memory as Lookup Table (LUT) inside Microcontroller (MCU). The low pass filter and temperature compensation block are used to adjust the raw data to the proper value. In addition, the redundancy mode is designed as a safety enhancement that alerts the faults during the positioning process, as briefly illustrated in Figure V.1. Two nodes are on behalf of two channels, carried the inclination data from 2 accelerometers. The fault can be detected via the difference data between 2 nodes or can be called as two channels by comparing with a threshold of 0.40°.

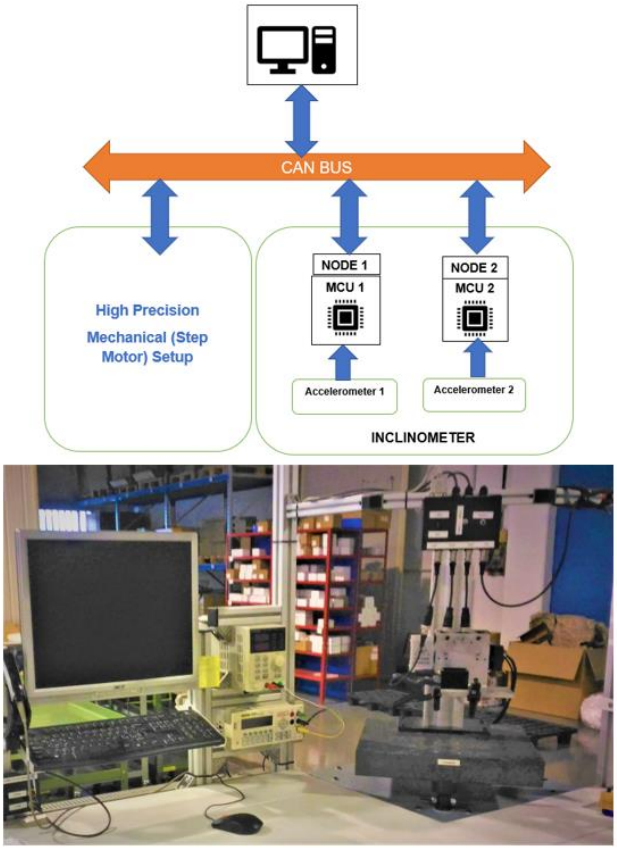

Figure V.1 *Redundancy structure for orientation system and real mechanical setup*

V.2 Low-pass filter and temperature compensation

V.2.1 LP filter

The same type of digital LP filter is implemented for accelerometer as described in section IV.1.
Figure V.2 shows the application for a sampling rate of 50 Hz, and the cut-off frequency is about 10 Hz.

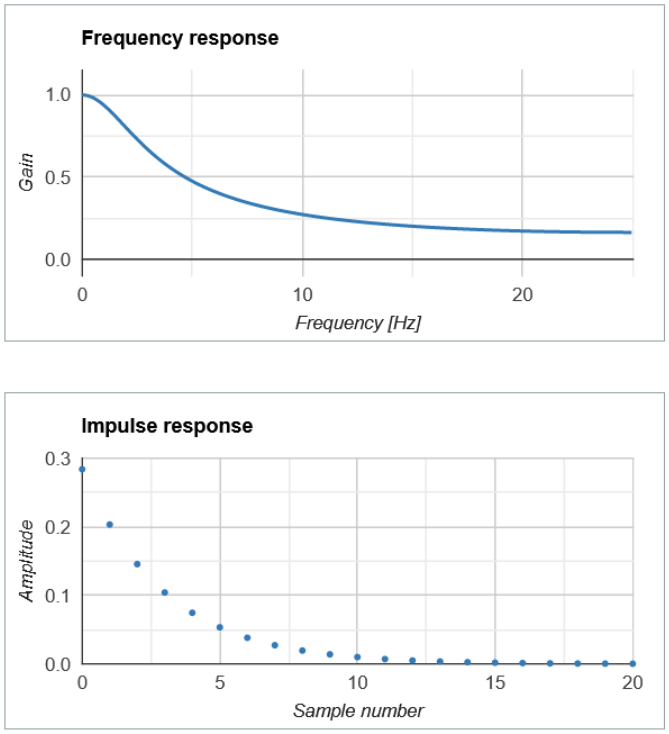

Figure V.2 *Frequency response and impulse response*

V.2.2 Temperature Compensation

Basically, the temperature change causes the variation of Zero-g offset like Figure V.3, so a simple but effective algorithm is used to adjust this value coherently. Usually, the accelerometer datasheet contains the coefficient of Zero-g offset change vs. temperature (TCO) in mg/°C. The accelerometer

offset temperature coefficient describes the deviation from the true value due to temperature changes from a nominal 25^0C condition.
The offset variation is called a bias which results from the product of TCO and temperature variation from 25°C.

bias = TC0(T_now-25) (V.1)

Where T_now is the current temperature.

In this way, the bias is always updated based on temperature variation to be removed from the raw acceleration.

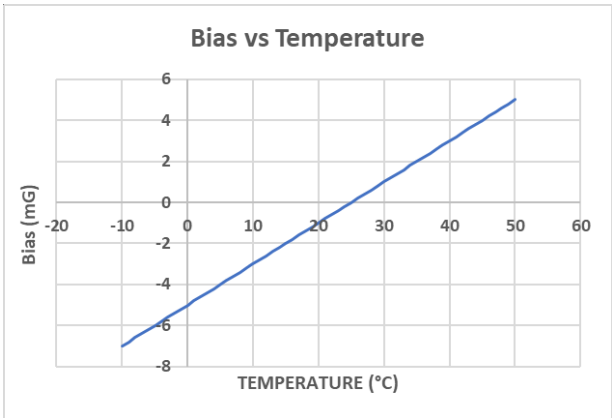

Figure V.3 *Bias vs Temperature Chart*

For high accuracy of thermal calibration, the sensor circuit is calibrated by the climatic chamber (Figure V.4), which has electronic microprocessor temperature controller. The chamber has temperature range from -40°C to +120 °C. The temperature change rate is about 5.0°C/min for heating and about 1.2°C/min for cooling.

The temperature adjustment was carried out to determine bias or characterization values for the platform.

- Procedures:

Step1: The sensor circuit was put inside the climatic chamber.

Step2: The chamber is maintained at 25^0C for 10 minutes, then the acceleration value is set to 0.

Step 3: The chamber temperature is decreased to 0^0C for another 30 minutes. Next, the temperature is decreased to -10^0. The offset values are recorded from each range.

Step 4: At this step, the temperature is adjusted from -10^{0}C to 70^{0}C with 10^{o}C steps. At each step, the temperature was kept stable for 40 minutes. The calibration results to determine new offsets, characterization values for the sensor circuit. To make modifications, the calibration process is repeated one more time to ensure the adjustments worked correctly.

For each range, the bias is calculated with mg/^{0}C and stored in system memory

$$B_n = \frac{\Delta A}{\Delta T} = \frac{A_{Tn} - A_{Tn-1}}{T_n - T_{n-1}} \qquad (V.2)$$

Where:

B_n is the bias at each adjustment step of temperature.

T_n and T_{n-1} are the temperatures at the current step and the previous step.

A_{Tn} and A_{Tn-1} are the calculated sensor error are the temperature at the current step and the previous step respectively.

With this technique, the bias is appropriately removed from acceleration data.

Figure V.4 *Climatic Chamber*

V.3 LUT filter

Figure V.5 shows the direction of the accelerometer from the top of view in this project. The LUT method imports the angle of inclination and its corresponding acceleration. After calibration, each time the sensor reaches the sensing acceleration of the x or y-axis, it will provide the corresponding orientational angle of roll or pitch based on the LUT data.

In this method, the acquisition values from Z-axis are ignored, the LUT filter only records the acceleration from X and Y axis independently.

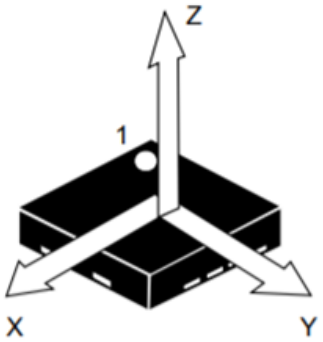

Figure V.5 *(Top view) direction of the accelerometer*

The method requires an accurate reference for the calibration. Therefore, an oriental motor for the industry is selected and verified by protractor 360^0 to assure its precision which is popularly applied to Inertial measuring units (IMU) (Lukáš, Jozef, Ľuboš, Peter, 2012).

- Calibration process:

The technique procedures are shown in Figure V.6 and Figure V.7. The inclinometer is mounted on the stepper motor. The Motor rotates at a specified resolution of step. During motor rotation, the MCU records the angle and corresponding acceleration value after a low pass filter. Roll and pitch data are calibrated separately then stored in 2 independent tables. In this way, the LUT filter contains all the calibration values.

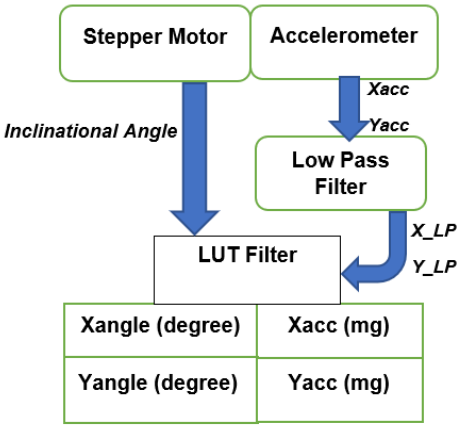

Figure V.6 *Calibration setup of inclinometer*

- Operating Process

After the calibration part, the tilt will be detected via acceleration values. The accelerometer sends the acquisition data to a low pass filter, and then the data are compensated with the temperature change before entering to LUT filter. Finally, the inclination angle is accomplished according to the memorized table.

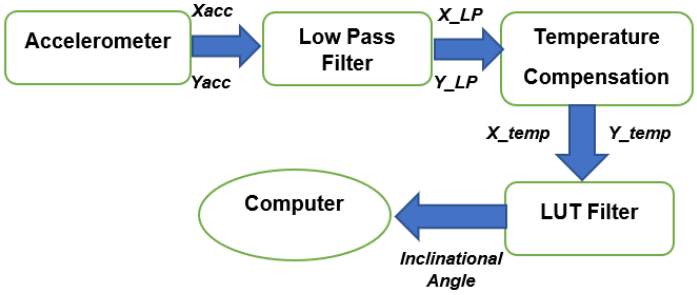

Figure V.7 *Operating Process of inclinometer*

Where: Xacc, Yacc are the accelerometer acquisition on X-axis and Y-axis, respectively.

X_LP, Y_LP are the filtered value from X-axis and Y-axis, respectively, after Low Pass Filter.

X_temp, Y_temp are the outputs of temperature compensation

Inclinational Angle is the tilt of the X-axis and Y-axis, with respect to the Earth frame

- Data linearization

When the acquisition value falls between 2 recorded data, the firmware includes an algorithm to calculate the gap between real data and two acceleration points before and after, then equalizes the measured data with the closest point (Figure V.8).

The distance between 2 consecutive acceleration Xn_{-1} and X_n is computed to seek the middle point between them. I_{n-1} and I_n are two corresponding inclination of X_{n-1} and X_n respectively. The lowest resolution of inclinator is 0,001°.

$$\Delta X = \frac{X_n - X_{n-1}}{2} \qquad (V.3)$$

- If $|X_{LP}| < |X_{n-1} + \Delta X/2|$ → Inclination = I_{n-1}
- If $|X_{LP}| > |X_{n-1} + \Delta X/2|$ → Inclination = I_n

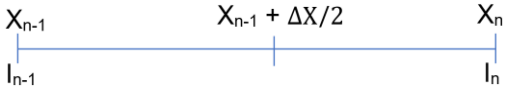

Figure V.8 *Two consecutive points in LUT*

- The architecture of system flash memory

The calibration data are stored into flash memory of MCU-STM32 from address 0x0800 0000 to 0x0801 FFFF as shown in Figure V.9. Here, the Cyclic Redundancy Check (CRC) has the mission to verify data transmission or storage integrity. In addition, CRC computes the signature of the application software during runtime, to be compared with a reference signature generated at link-time and stored at a given memory location.
Bootloader manages the erase operation of this location before writing in a Data memory location. Data on temperature calibration and accelerations with coherent inclinations are stored in flash. This technique guarantees the long-term performance of the sensor.

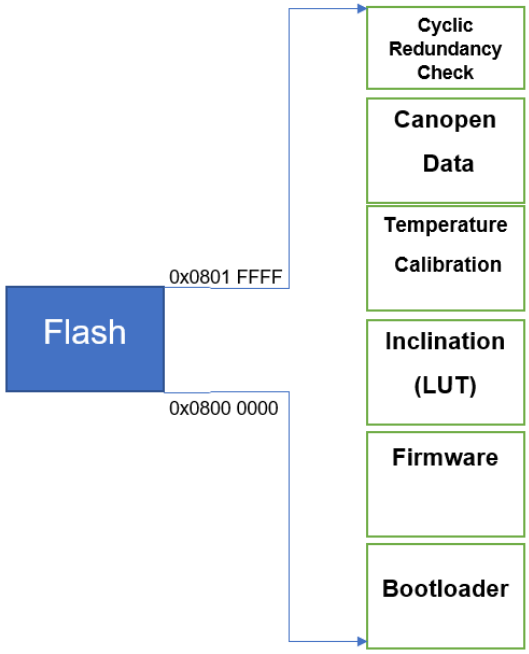

Figure V.9 *Stored data architecture in flash*

V.4 Redundant function

V.4.1 Redundancy architecture

In the bad cases, faults in position measurement pose a severe hazard during dynamic positioning (Rogne, Johansen and Fossen, 2014). Therefore, the redundancy plays a critical role in the inclinometer safety. Dual accelerometers transmit the data which are used for the inclination measurements then sent out via two nodes. At this point, two channels provide oriental angles as illustrated in Figure V.10. To guarantee the safety of the system, the difference between 2 orientation angles from 2 nodes (Δangle) cannot exceed a working threshold (Δth). Otherwise, the error message will be sent to the user.

The redundant mode must guarantee stable performance from both 2 sensor channels based on Δth. Under the same operating condition, 2 angles values supposed to be the same or close to each other.

- If Δangle is greater than Δth frequently, it indicates the less accuracy of the inclinometer at that period and the acquisition data is trustless.

• Without redundant mode, it is difficult for the user to realize whether the inclinometer is working properly or not.

The Δth is selected with value 0.40°. The maximum error of each inclinometer channel is 0.20°. Here, we take into account that when both two sensor channels get the maximum error. Considering the worst case, the allowed maximum difference is equal to 0.4° when one node has less value than the reference 0.20^0; another node exceeds value than the reference 0.20^0

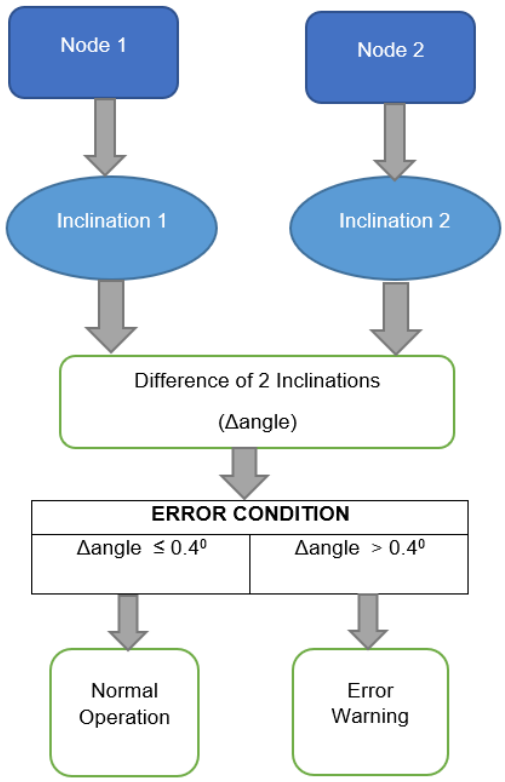

Figure V.10 *Redundancy chart*

V.4.2 Error solutions

When the positioning warning frequently occurs more than 110 times for 10 minutes, the priority solution is to stop the sensor motion for 45 seconds (Figure V.11). Perhaps, the data from one node arrives in delay. After the waiting period, if the inclination difference from 2 nodes comes back to lower

than 0.4°, it means that the problem is solved. Otherwise, the power supply should be checked, and the inclinometer supposed to be reset. They are two fundamental errors that can be identified easily by a redundant function as described in Table V.1.

Table V.1 *Error warning*

Error type	Solution
Data Delay	Rest the inclinometer at static state for 45 seconds (s) → System comes back to work normally.
Error of physical material (power supply problem)	Checking power supply Reset the system.

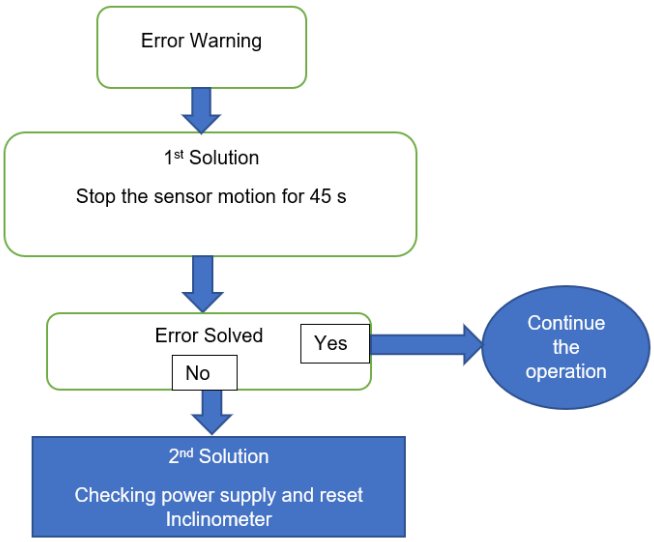

Figure V.11 *Error solution diagram*

V.5 Experimental analysis

In the experiment, a robust setup is constructed accurately for the calibration as well as the acquisition of the proposed inclinometer as shown in Figure V.12. The sensor involved in acquiring data for the experiments is the accelerometer LIS2DW12 with the Output Data Rate of 50Hz. This device is a system-in-package featuring a tri-axial digital linear acceleration sensor with a 16-bit resolution and selectable full-range scale ±2 to ±16 g full scale. The NUCLEO-F103RB (STMicroelectronics, 2019) with a maximum clock frequency of 72 MHZ is used to implement the LUT filter into an external MCU STM32F103C8T6 (STMicroelectronics, 2015) via ARM's Serial Wire Debug (SWD). This MCU with Flash Memory of 64 kB is embedded in the inclinometer.

The sensor is interfaced to the MCU development via a Serial Peripheral Interface (SPI) communication line in full-duplex mode. The Controller Area Network open (CANopen bus) is used as communication protocol and device profile specification for the embedded network.

High precision and robust stepper motor: Vexta oriental motor DGM130R-ASAA (Oriental Motor, 2011), used as a reference. A metal piece is designed to handle the inclinometer appropriately, which is mounted on the stepper motor for left-right rotation.

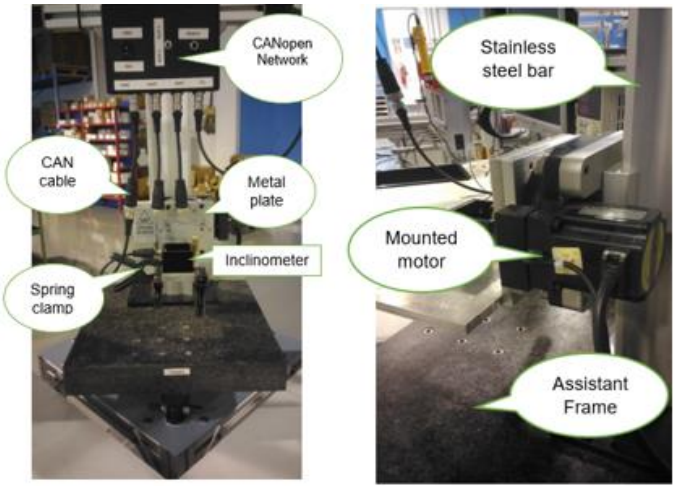

Figure V.12 *Inclinometer setup and mounted motor on setup*

The LUT algorithm is programmed into the inclinometer. After sending a message to activate, the microcontroller starts recording the X-axis for roll and Y-axis for pitch. In this way, the stepper motor motion and the LUT memorization are carried out simultaneously. At this point, the inclinometer will measure the inclinational angles corresponding to the value of the X and Y-axis in LUT. The cover of the inclinometer is made up of metallic to resist the vibration by its weight.

After the calibrating process, the setup will go around in a circle again to verify the performance of the calibrated inclinometer. The maximum tolerance is only allowed at 0.20. In the case the error evaluation exaggerates this tolerance, the inclinometer must be re-calibrated. In the experiment, the inclinometer is applied in the range from -90^0 to 90^0

The tests were carried out to inspect the stability and precision of the redundant inclinometer. All the errors were reported in absolute value for simple observation and analysis, based on the reference angle of the motor.

V.6 Experimental test

For stability examination, the setup is set at rotation speed of 80 ^{0}/s from -40^0 to 40^0. About 20 repetitive cycles are processed on X-axis and Y-axis as shown in Figure V.13 and Figure V.15. The data of the inclinometer appropriately follow the trend of the dynamic rotation with high accuracy.

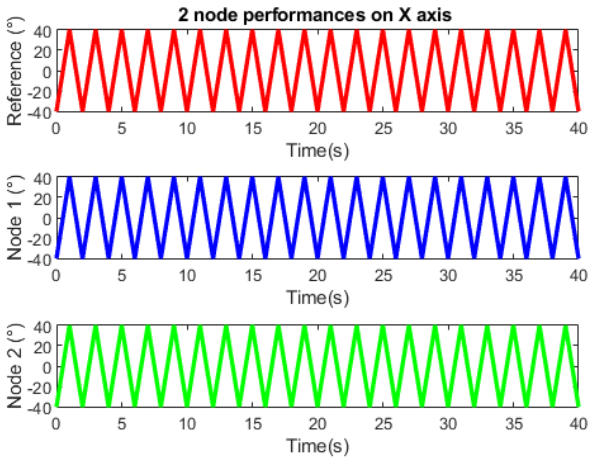

Figure V.13 *Inclination Detection on X-axis*

Figure V.14 demonstrates the absolute value of each node error to the reference inclination and Δangle between 2 nodes. Both 2 channels obtain the error under the allowable tolerance ($\leq 0.2^0$). In addition, the Δangle does not overcomes 0.4^0 as it is supposed to be, so the inclinometer works appropriately like the designed requirement.

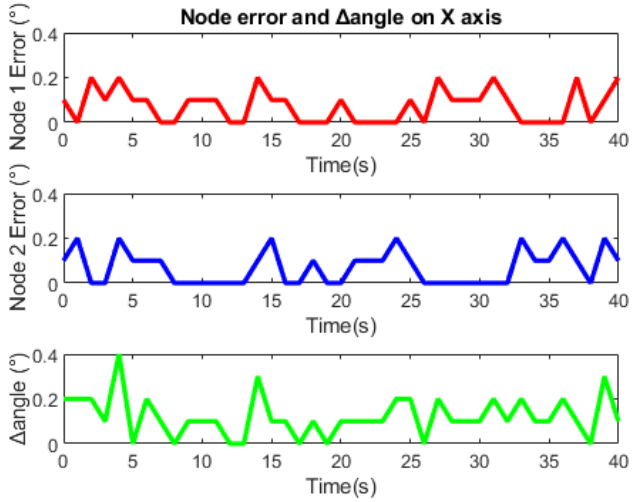

Figure V.14 *Node Error and Δangle on X-axis*

For the Y axis (pitch) detection, the setup remains the same rotation speed of 80 ^{0}/s like previous test, but in the range of -60^0 to 60^0. Similar to the X-axis (roll) tracking performance, both of 2 nodes track the angle coherently to the oriental reference as shown in Figure V.15, together with their error value and Δangle are conducted under the proper range like Figure V.16.

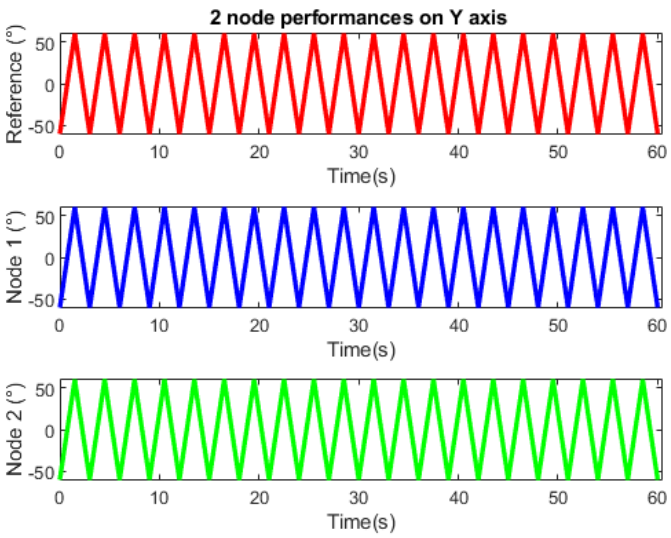

Figure V.15 *Inclination Detection on Y-axis*

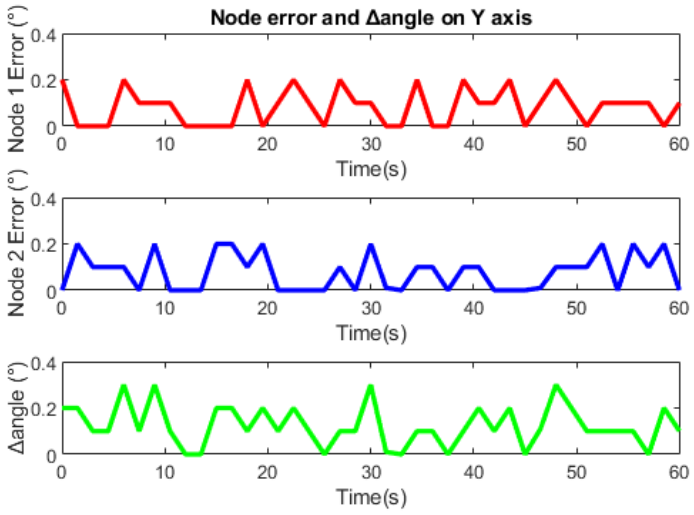

Figure V.16 *Node Error and Δangle on Y-axis*

The data from Table V.2 confirm the certainty and stability of the inclinometer. After 20 repetitive cycles, the mean value of both 2 axes are close to the true angle with narrow Std.Dev. There is no error warning, thanks to the precise execution. The maximum difference value between 2 nodes is always less than 0.2^0, so the system is always in normal operating condition.

Table V.2 *Measurement characterization of 20 cycles*

Axis	Reference (°)	Node 1 (°)		Node 2 (°)		2 Nodes Maximum difference (°)	Error Warning
		Mean (°)	Std.Dev (°)	Mean (°)	Std.Dev (°)		
X-axis (Roll)	-40	-40.15	0.11	-39.95	0.10	0.4	No
	40	40.05	0.09	40.15	0.08		
Y-axis (Pitch)	-60	-60.12	0.07	-60.11	0.09	0.3	No
	60	60.13	0.10	60.06	0.07		

V.7 Fault detection on real application

For 7 days, the designed inclinometer was tested in an excavator as support of excavation depth measurement control via the pitch angle (angle on Y-axis) of the mechanical arm. Figure V.17 illustrates the position of the testing sensor. Each day the sensor was in work for 3 hours, with 50 samples are extracted per second. Figure V.18 reports the number of detected errors per day. The inclinometer works well as the expectation. No error occurred except day 5 where the power supply was unstable because of a technical problem. Consequently, a fault detected thanks to the safety function between 2 nodes on Y-axis. Each node considered as a channel.

Figure V.17 *Testing Inclinometer in Excavator*

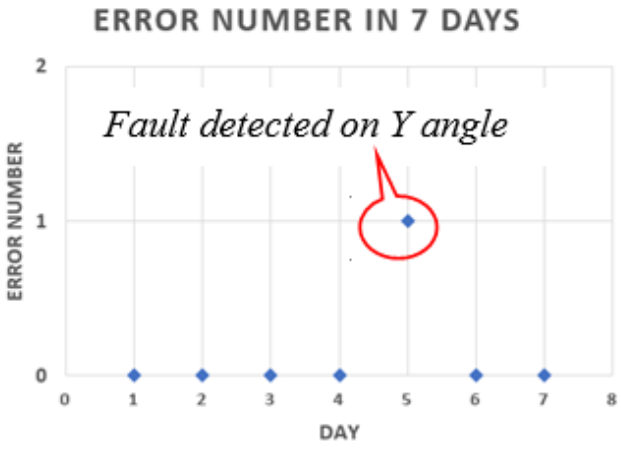

Figure V.18 *Error number for 7 days*

Figure V.19 shows the maximum of angle variation between 2 nodes, approximately 1°. The different measurement between 2 nodes is called as delta channel. In the fault case, the delta channel still can be a standard (less than 0.20°), but only for a short period then rises. This signal indicates that the system is in an unstable situation, and the users need to check the operating system to guarantee stability. The delta channel frequently surpasses 0.40° for 10 minutes. In this way, error detected, and the inclinometer was temporarily stopped and reset. After this period, the sensor comes back to work normally.

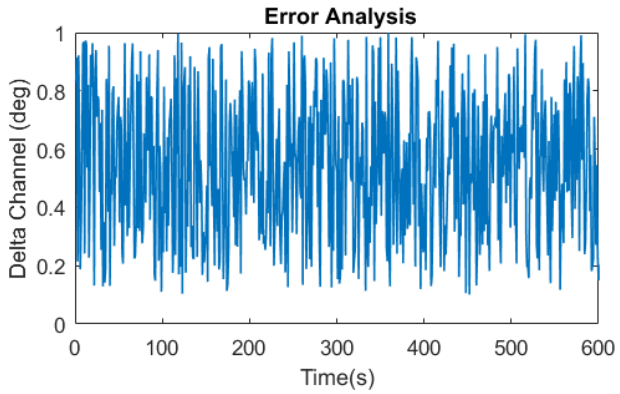

Figure V.19 *Variation of delta channel on Y-axis*

V.8 Conclusion for the industrial inclinometer system

A highly effective system for inclinometer was designed with a successful operation in both static and dynamic cases. The redundant mode guarantees the safety of oriental operation which is always ready to alert the users in the case of risk accuracy. As reported results in Table V.2, the redundant mode does not detect any error during the experiment, showed the robust and potent design of the inclinometer. In the real application with the excavator, the fault was detected thanks to the proposed safety function to resolve the technical problem. The proposed structure of the inclinometer is strongly recommended for the application in heavy industry with a practical method of orientation and long-term stability.

Conclusion

This work successfully designed the new algorithms for the optimization of orientation angle. With NMNI filter, the yaw/heading is detected without magnetometer and GPS presence, which relief the burden of system complexity and vulnerability. In addition, roll and pitch in Madgwick and Mahony filter are improved apparently with less noise and superior accuracy since the gyroscope drift is eliminated. With the economy concern of inclinometer company, the MEMS accelerometer was deeply researched and the OACP filter was proposed. The vibration threshold and the update threshold procedure help the system to minimize the noise impact on roll and pitch.

In the last chapter, the research activity in the company was demonstrated. robust technique implemented into the inclinometer based on Lookup Table (LUT) Filter. The filter memorizes the acceleration data corresponding to the angle of inclination as an ideal curve graph of MEMS accelerometer. This technique works as not only acceleration calibration but also a powerful tool of inclination measurement. A high precision robust setup for inclinometer calibration and metrology was built. The proposed method is applied to two axis-inclinometer with a maximum error of 0.2^{o}. The full redundancy with 2 angle channels can guarantee the safety the inclinometer function. The experiment includes both static and dynamic procedures to justify the accuracy as well as the stability of the operating system.

In the future, the combination between NMNI algorithm and OACP algorithm will implemented into the inclination system to compare the efficiency of this approach with the current version. Moreover, the gyroscope and magnetometer will be considered also in the redundancy operation for further development of the orientation sensor.

References

Hoang, M.L., Iacono, S.D., Paciello, V. and Pietrosanto, A. (2021). Measurement Optimization for Orientation Tracking Based on No Motion No Integration Technique. IEEE Transactions on Instrumentation and Measurement, 70, pp.1–10. DOI: 10.1109/tim.2020.3035571

Hoang, M.L., Carratù, M., Paciello, V. and Pietrosanto, A. (2021). Body Temperature—Indoor Condition Monitor and Activity Recognition by MEMS Accelerometer Based on IoT-Alert System for People in Quarantine Due to COVID-19. Sensors, 21(7), p.2313. DOI: 10.3390/s21072313

Carratu, M., Iacono, S.D., Long Hoang, M. and Pietrosanto, A. (2019). Energy characterization of attitude algorithms. 2019 IEEE 17th International Conference on Industrial Informatics (INDIN), pp. 1585-1590. DOI: 10.1109/INDIN41052.2019.8972300.

Harindranath, A. and Arora, M. (2018). MEMS IMU Sensor Orientation Algorithms-Comparison in a Simulation Environment. *2018 International Conference on Networking, Embedded and Wireless Systems (ICNEWS), pp. 1-6*.

Huyghe, B., Doutreloigne, J. and Vanfleteren, J. (2009). 3D orientation tracking based on unscented Kalman filtering of accelerometer and magnetometer data. *2009 IEEE Sensors Applications Symposium, pp. 148-152*.

Lan, G., Bu, Y., Liang, J. and Hao, Q. (2016). Action synchronization between human and UAV robotic arms for remote operation. *2016 IEEE International Conference on Mechatronics and Automation , pp. 2477-2481*.

Kong, X. (2004). INS algorithm using quaternion model for low cost IMU. *Robotics and Autonomous Systems*, 46(4), pp.221–246.

Qinglei, G., Huawei, L., Shifu, M. and Jian, H. (2007). Design of a Plane Inclinometer Based on MEMS Accelerometer. *2007 International Conference on Information Acquisition*, pp. 320-323.

Wang, J., Gao, G. and Liu, P. (2010). The study on lange-angle CANBUS 2-axis inclinometer of rotary drilling rig. *2010 2nd IEEE International Conference on Information Management and Engineering , pp. 95-97*.

Da-wei, L. and Tao, G. (2011). Design of Dual-axis Inclinometer Based on MEMS Accelerometer. *2011 Third International Conference on Measuring Technology and Mechatronics Automation , pp. 959-961*.

Helbling, E.F., Fuller, S.B. and Wood, R.J. (2014). Pitch and yaw control of a robotic insect using an onboard magnetometer. *2014 IEEE International Conference on Robotics and Automation (ICRA) , pp. 5516-5522,*.

Shi, G., Li, X. and Jiang, Z. (2018). An Improved Yaw Estimation Algorithm for Land Vehicles Using MARG Sensors. *Sensors*, 18(10), p.3251.

Hoang, M.L., Iacono, S.D., Paciello, V. and Pietrosanto, A. (2021). Measurement Optimization for Orientation Tracking Based on No Motion No Integration Technique. IEEE Transactions on Instrumentation and Measurement, 70, pp.1–10. DOI: 10.1109/tim.2020.3035571

Carratu, M., Iacono, S.D., Pietrosanto, A. and Paciello, V. (2019). IMU self-alignment in suspensions control system. *2019 IEEE International Instrumentation and Measurement Technology Conference (I2MTC) pp. 1-6*.

Wahyudi, Listiyana, M.S., Sudjadi and Ngatelan (2018). Tracking Object based on GPS and IMU Sensor. *2018 5th International Conference on Information Technology, Computer, and Electrical Engineering (ICITACEE) , pp. 214-218*.

Damani, A., Shah, H., Shah, K. and Vala, M. (2015). Global Positioning System for Object Tracking. *International Journal of Computer Applications*, 109(8), pp.40–45.

Hoang, M.L. and Pietrosanto, A. (2021). A New Technique on Vibration Optimization of Industrial Inclinometer for MEMS Accelerometer Without Sensor Fusion. IEEE Access, 9, pp.20295–20304. DOI: 10.1109/ACCESS.2021.3054825.

Hoang, M.L. and Pietrosanto, A. (2021). New Artificial Intelligence Approach to Inclination Measurement based on MEMS Accelerometer. IEEE Transactions on Artificial Intelligence, 2021. DOI: 10.1109/TAI.2021.3105494.

Hoang, M.L. and Pietrosanto, A. (2021). A Robust Orientation System for Inclinometer With Full-Redundancy in Heavy Industry. IEEE Sensors Journal, 21(5), pp.5853–5860. DOI: 10.1109/JSEN.2020.3040374.

Hoang, M.L., Pietrosanto, A., Iacono, S.D. and Paciello, V. (2020). Pre-Processing Technique for Compass-less Madgwick in Heading Estimation for Industry 4.0. 2020 IEEE International Instrumentation and Measurement Technology Conference (I2MTC), pp. 1-6. DOI: 10.1109/I2MTC43012.2020.9128969

Christopher J. F. (2010) . AN-1057: Using an Accelerometer for Inclination Sensing. Analog device

Promrit, P., Chokchaitam, S. and Ikura, M. (2018). In-Vehicle MEMS IMU Calibration Using Accelerometer. *2018 IEEE 5th International Conference on Smart Instrumentation, Measurement and Application (ICSIMA), pp. 1-3*.

Cocco, L. and Rapuano, S. (2007). Accurate Speed Measurement Methodologies for Formula One Cars. *2007 IEEE Instrumentation & Measurement Technology Conference IMTC 2007 , pp. 1-6*.

STMicroelectronics. (2019). LIS2DW12 MEMS digital output motion sensor: high-performance ultra-low-power 3-axis "femto" accelerometer.

Hu, F. *et al.* (2019). An improved method for the magnetometer calibration based on ellipsoid fitting. *2019 12th International Congress on Image and Signal Processing, BioMedical Engineering and Informatics (CISP-BMEI), pp. 1-5*.

Maxudov, N., Ercan, A. O. and Erdem, A. T. (2015). Effect of camera-IMU displacement calibration error on tracking performance. *2015 IEEE International Conference on Image Processing (ICIP)*, pp. 4476-4480.

Ariffin, N. H., Arsad, N. and Bais, B. (2016). Low-cost MEMS gyroscope and accelerometer implementation without Kalman Filter for angle estimation. *2016 International Conference on Advances in Electrical, Electronic and Systems Engineering (ICAEES)*, pp. 77-82.

Euston, M. *et al.* (2008). A complementary filter for attitude estimation of a fixed-wing UAV. *2008 IEEE/RSJ International Conference on Intelligent Robots and Systems*, pp. 340-345.

Brunner, T. *et al.* (2015). Quaternion-based IMU and stochastic error modeling for intelligent vehicles. *2015 IEEE Intelligent Vehicles Symposium (IV)*, pp. 877-882.

Diebel.J. (2006). Representing attitude: Euler angles, unit quaternions, and rotation vectors. Matrix, 15–16.

Kuipers, J. B. (2020). *Quaternions and rotation sequences: A primer with applications to orbits, aerospace and virtual reality*. Princeton, NJ: Princeton University Press. doi: 10.2307/j.ctvx5wc3k.

Madgwick, S. O. H., Harrison, A. J. L. and Vaidyanathan, A. (2011). Estimation of IMU and MARG orientation using a gradient descent algorithm. *2011 IEEE International Conference on Rehabilitation Robotics*, 2011, , pp. 1-7.

Sarbishei, O. (2016). On the accuracy improvement of low-power orientation filters using IMU and MARG sensor arrays. *2016 IEEE International Symposium on Circuits and Systems (ISCAS)*, pp. 1542-1545.

Admiraal, M., Wilson, S. and Vaidyanathan, R. (2017). Improved formulation of the IMU and MARG orientation gradient descent algorithm for motion tracking in human-machine interfaces. *2017 IEEE International Conference on Multisensor Fusion and Integration for Intelligent Systems (MFI)*, pp. 403-410.

Selvarajan, M. and Ananda, C. M. (2016). Quaternion based pointing algorithm for two-axis gimbal of micro aerial vehicles. *2016 IEEE International Conference on Recent Trends in Electronics, Information & Communication Technology (RTEICT)*, pp. 1335-1339.

Xing, H. *et al.* (2019). Quaternion-based complementary filter for aiding in the self-alignment of the MEMS IMU. *2019 IEEE International Symposium on Inertial Sensors and Systems (INERTIAL)*, pp. 1-4.

NGA and the U.K.'s Defence Geographic Centre (DGC). (2015). *The World Magnetic Model*. [Online]. Available: http://www.ngdc.noaa.gov/geomag/WMM

Ludwig, S. A. and Burnham, K. D. (2018). Comparison of Euler estimate using extended Kalman filter, madgwick and Mahony on quadcopter flight data. *2018 International Conference on Unmanned Aircraft Systems (ICUAS)*, pp. 1236-1241.

Chen, T., Hu, W. and Sun, R. (2010). Displacement Measurement Algorithm Using Handheld Device with Accelerometer. *2010 Asia-Pacific Conference on Wearable Computing Systems*, pp.122–126.

STMicroelectronics. (2015). INEMO inertial module: 3D accelerometer, 3D gyroscope, 3D magnetometer - Data Sheet.

STMicroelectronics. (2015). Ultra-low-power Arm® Cortex®-M4 32-bit MCU+FPU, 105 DMIPS, 512KB Flash/96KB RAM, 11 TIMs, 1 ADC, 11 comm. Interfaces.

STMicroelectronics. (2018). STM32F401xB/C and STM32F401xD/E advanced Arm®-based 32-bit MCUs.

STMicroelectronics. (2018). STM32 Nucleo-64 boards - Product Specifications.

STMicroelectronics. (2017). STM32 Nucleo-64 boards - User Manual, December.

STMicroelectronics. (2016). LSM9DS1 adapter board for a standard DIL24 socket.

Rollins, R. B. (2000). Pan-Tilt Unit (Model PTU) User's Manual - Version 1.14.

Madgwick, S.O.H., Harrison, A.J.L. and Vaidyanathan, R. (2011). Estimation of IMU and MARG orientation using a gradient descent algorithm.

2011 IEEE International Conference on Rehabilitation Robotics, pp.1–7.

Jaber, H. and Frye, M. (2020). Laguerre Polynomials and Gradient Descent Approach for Linear Quadratic Optimal Control. *2020 7th International Conference on Electrical and Electronics Engineering (ICEEE)*, pp.281–284.

Shobha, G. and Rangaswamy, S. (2018). Chapter 8 - Machine Learning, Handbook of Statistics, Elsevier, Volume 38, pp. 197-228.

Kingma, D. P. and Ba, J. (2014). Adam: A method for stochastic optimization arXiv [cs.LG].

Sriram, R. D. (1997). Neural Networks. Intelligent Systems for Engineering in Springer London, pp. 471–542.

Pedregosa *et al.*, (2011) Scikit-learn: Machine Learning in Python. JMLR 12, pp. 2825-2830, 2011.

Abadi, Mart'in et al., (2016). Tensorflow: A system for large-scale machine learning. In 12th $USENIX$ Symposium on Operating Systems Design and Implementation ($OSDI$ 16). pp. 265–283.

Hoang, M.L., Carratu, M., Paciello, V. and Pietrosanto, A. (2020). A new Orientation Method for Inclinometer based on MEMS Accelerometer used in Industry 4.0. 2020 IEEE 18th International Conference on Industrial Informatics (INDIN), 2020, pp. 177-181. DOI: doi: 10.1109/INDIN45582.2020.9442189.

Lukáš, P., Jozef, R., Ľuboš, C., Peter, H., (2012). Integration of Inertial Measuring Unit Platform into MATLAB Simulink. 9th IFAC Symposium Advances in Control Education, Volume 45, Issue 11, Russia, June, pp. 19-21.

Rogne, R.H., Johansen, T.A. and Fossen, T.I. (2014). Observer and IMU-based detection and isolation of faults in position reference systems and gyrocompasses with dual redundancy in dynamic positioning. 2014 IEEE Conference on Control Applications (CCA), pp.83–88.

STMicroelectronics. (2019). STM32 Nucleo-64 Boards—Product Specifications, Geneva, Switzerland.

STMicroelectronics. (2015). STM32F103xB, Medium-density performance line ARM®-based 32-bit MCU with 64 or 128 KB Flash, USB, CAN, 7 timers, 2 ADCs, 9 com. Interfaces.

Oriental Motor Co., Ltd. (2011). Hollow Rotary Actuators DG Series DG85, DG130, DG200, Ueno, Tokyo.

La borsa di dottorato è stata cofinanziata con risorse del
Programma Operativo Nazionale Ricerca e Innovazione 2014-2020 (CCI 2014IT16M2OP005),
Fondo Sociale Europeo, Azione I.1 "Dottorati Innovativi con caratterizzazione Industriale"

UNIONE EUROPEA
Fondo Sociale Europeo

Ministero dell'Istruzione, dell'Università e della Ricerca

PON RICERCA E INNOVAZIONE